# The proteasomal deubiquitinating enzyme PSMD14 regulates macroautophagy by controlling Golgi-to-ER retrograde transport

Bustamante HA[1,2], Cereceda K[3], González AE[1,4], Valenzuela GE[5,6], Cheuquemilla Y[6], Hernández S[3], Arias-Muñoz E[3], Cerda-Troncoso C[3], Bandau S[8], Soza A[3], Kausel G[5], Kerr B[3], Mardones GA[1,7], Cancino J[3], Hay RT[8], Rojas-Fernandez A[6,8¥], Burgos PV[3,9¥]

[1]Instituto de Fisiología, Facultad de Medicina, Universidad Austral de Chile, 5110566, Valdivia, Chile

[2]Instituto de Microbiología Clínica, Facultad de Medicina, Universidad Austral de Chile, 5110566, Valdivia, Chile

[3]Centro de Biología Celular y Biomedicina (CEBICEM), Facultad de Medicina y Ciencia, Universidad San Sebastián, Lota 2465, 7510157, Santiago, Chile

[4]Institute of Biochemistry II, School of Medicine, Goethe University Frankfurt, Theoder-Stern-Kai 7, 60590, Frankfurt am Main, Germany

[5]Instituto de Bioquímica y Microbiología, Facultad de Ciencias, Universidad Austral de Chile, 5110566, Valdivia, Chile.

[6]Instituto de Medicina & Centro Interdisciplinario de Estudios del Sistema Nervioso (CISNe), Universidad Austral de Chile, 5110566, Valdivia, Chile.

[7]Centro Interdisciplinario de Estudios del Sistema Nervioso (CISNe), Universidad Austral de Chile, 5110566, Valdivia, Chile.

[8]Centre for Gene Regulation and Expression, College of Life Sciences, University of Dundee, DD1 4HN, Dundee, United Kingdom.

[9]Centro de Envejecimiento y Regeneración (CARE-UC), Facultad de Ciencias Biológicas, Pontificia Universidad Católica de Chile, 83330023, Santiago, Chile

**Correspondence to:**

[¥] Patricia Burgos, PhD. Centro de Biología Celular y Biomedicina, Facultad de Medicina y Ciencia, Universidad San Sebastián, Lota 2465, Santiago 7510157, Chile. Email: patricia.burgos@uss.cl

[¥]Alejandro Rojas-Fernández, PhD. Instituto de Medicina & Centro Interdisciplinario de Estudios del Sistema Nervioso (CISNe), Universidad Austral de Chile, Valdivia 5110566, Chile. Email: alejandro.rojas@uach.cl

**ABSTRACT**

Ubiquitination regulates several biological processes. Here, we search for ubiquitin-related genes implicated in protein membrane trafficking performing a High-Content siRNA Screening including 1,187 genes of the human "ubiquitinome" using Amyloid Precursor Protein (APP) as a reporter. We identified the deubiquitinating enzyme PSMD14, a subunit of the 19S regulatory particle of the proteasome, specific for K63-Ub chains in cells, as a novel key regulator of Golgi-to-endoplasmic reticulum (ER) retrograde transport. Silencing or pharmacological inhibition of PSMD14 caused a robust and rapid inhibition of Golgi-to-ER retrograde transport which leads to a potent blockage of macroautophagy by a mechanism associated with the retention of Atg9A and Rab1A at the Golgi apparatus. Because pharmacological inhibition of the proteolytic core of the 20S proteasome did not recapitulate these effects, we concluded that PSMD14, and their K-63-Ub chains, act as a crucial regulator factor for macroautophagy by controlling Golgi-to-ER retrograde transport.

Keywords: PSMD14, Ubiquitin, Retrograde, Trafficking, APP

## Introduction

Several post-translational modifications (PTMs) contribute to membrane transport [1,2]. Among these, ubiquitination acts as a relevant player in protein membrane trafficking [3–5] participating as an important protein localization signal [3,6–8]. However, to date most studies have focused on its role in endocytosis, particularly in the inclusion of cargoes in intraluminal vesicles (ILVs) of multivesicular bodies (MVBs) [9–11] such as cell-surface receptors [12]. Ubiquitination is a regulated post-translational modification that conjugates ubiquitin (Ub) to lysine (K) residues and is involved in many cellular pathways including the degradation of target proteins through the proteasomes and autophagy [13,14]. Ubiquitin modification is a cascade of reactions catalyzed by three classes of enzymes (E1, E2 and E3). An ATP dependent E1 activating enzymes first forms a covalent intermediate with ubiquitin, followed by the transfer of Ub to E2 conjugating enzymes and finally the covalent attachment of Ub to a K residue in the target protein by E3 Ub ligases [15]. Ubiquitination is a reversible reaction, with specific deubiquitinating enzymes (DUBs) that catalyze the removal of Ub-moieties for their recycling. DUBs serve to counterbalance ubiquitination reactions within the cell, thus dynamically contributing to the regulation of various cellular processes, such as endosomal sorting [11,16–18].

Ub increases proteome complexity, providing an additional surface for protein-protein interactions and functional regulation [19,20]. Ub-modified proteins and Ub chains are recognized by several Ub receptors including a family of specialized proteins carrying Ub binding domains (UBDs). To date, over 20 UBD families have been identified and characterized in mammals participating in recognition of Ub monomers or Ub chains on specific substrates [4,14,21]. Together, the Ub network offers a variety of choices to modulate cellular processes including protein membrane trafficking. However, the contribution of the ubiquitinome regarding their impact in intracellular membrane trafficking is not yet fully understood.

To investigate the contribution of most of the members of the ubiquitinome in protein membrane trafficking, we performed High-Content siRNA Screening (HCS) including 1,187 genes of the human “ubiquitinome”. For this screening we used a stable cell line expressing Amyloid Precursor Protein (APP) fused to EGFP. APP was the protein selected as target because it traffics dynamically through the secretory and endocytic pathways

77 containing specific sorting signal motifs [22–24] and specific lysine residues targets of
78 ubiquitination [25–28]. We thus identified the deubiquitinating (DUB) enzyme PSMD14, a
79 subunit of the 19S regulatory particle (RP) of the proteasome, as a crucial player of Golgi-
80 to-Endoplasmic reticulum (ER) retrograde transport. The DUB enzyme PSMD14 has been
81 shown to be specific for K63-Ub chains in cells [29]. Here, we found that the inhibition of its
82 activity blocks Golgi-to-ER retrograde transport causing the swelling of the Golgi
83 apparatus. Also, we found that PSMD14 inhibition acts as a potent blocker of
84 macroautophagy as a result of its negative impact in Golgi-to-ER retrograde transport.
85 Inhibition of the proteolytic core of the 20S proteasome by MG132 did not recapitulate
86 these effects, indicating that the 19S RP plays a role on macroautophagy by controlling
87 membrane trafficking at the early secretory pathway.

## Results

***High-Content siRNA Screening revealed PSMD14 deubiquitinating enzyme as a novel regulator of protein trafficking.***

To investigate the contribution of the ubiquitinome in protein membrane trafficking, we performed an automated HCS using a human small interfering RNA (siRNA) "ubiquitinome" library, consisting of 1,187 siRNA duplex pools targeting all known and predicted Ub-genes. This library, used previously in mammalian screening assays [30,31] includes E1 activating enzymes (0.8%), E2 conjugating enzymes (4.7%), E3 Ub ligases (61.2%), UBD-containing proteins (12.8%), DUBs (8.8%), SUMO-specific proteases (SENPs) (0.2%) and others (11.4%) (Fig. 1A). We used this library to identify novel regulators of protein membrane trafficking using an H4 neuroglioma cell line stably expressing APP-EGFP, a cell line previously characterized and used in siRNAs knockdown experiments [24,32,33]. We standardized the basal (background) and maximum fluorescence intensity by analyzing total fluorescence of silenced and non-silenced APP-EGFP, respectively. A reduction in total fluorescence intensity from 100% to 6% was observed with the EGFP siRNA, compared to the Non-Target (NT) siRNA with a Z factor of 0.69 (Fig. 1B). Representative images of basal and maximum levels of total fluorescence intensity in reporter cells are shown in Fig. 1C. Cells were further assessed with a primary siRNA screening consisting of a pool of four-different siRNA duplexes for each of the 1,187 genes selected, each siRNA targeting a distinct region to minimize their off-targets effects [34]. Fig. 1D shows a summary of the results with all siRNA pools tested and normalized in respect to the expression of the NT siRNA. Among the 1,187 tested genes, we found that the highest total fluorescence increase (4.15-fold increase) corresponded to protein PSMD14 (POH1, also known as Rpn11/MPR1/SS13/CepP1) (Fig. 1D), a subunit of the 19S regulatory particle (RP) of the proteasome, which has DUB activity [35,36]. Representative images of reporter cells knock-down (KD) of PSMD14 in comparison to cells transfected with NT siRNA are shown in Fig. 1E. Further, we validated these results analyzing the effect of PSMD14 KD on the levels of full-length endogenous APP in parental H4 cells by western blot. The effect of all four PSMD14 siRNAs in KD cells tested on endogenous APP levels are shown in Fig. 2A (first panel, lanes 3-6) and compared to un-transfected cells (Mock) or cells transfected with NT siRNA (Fig. 2A, first panel, lanes

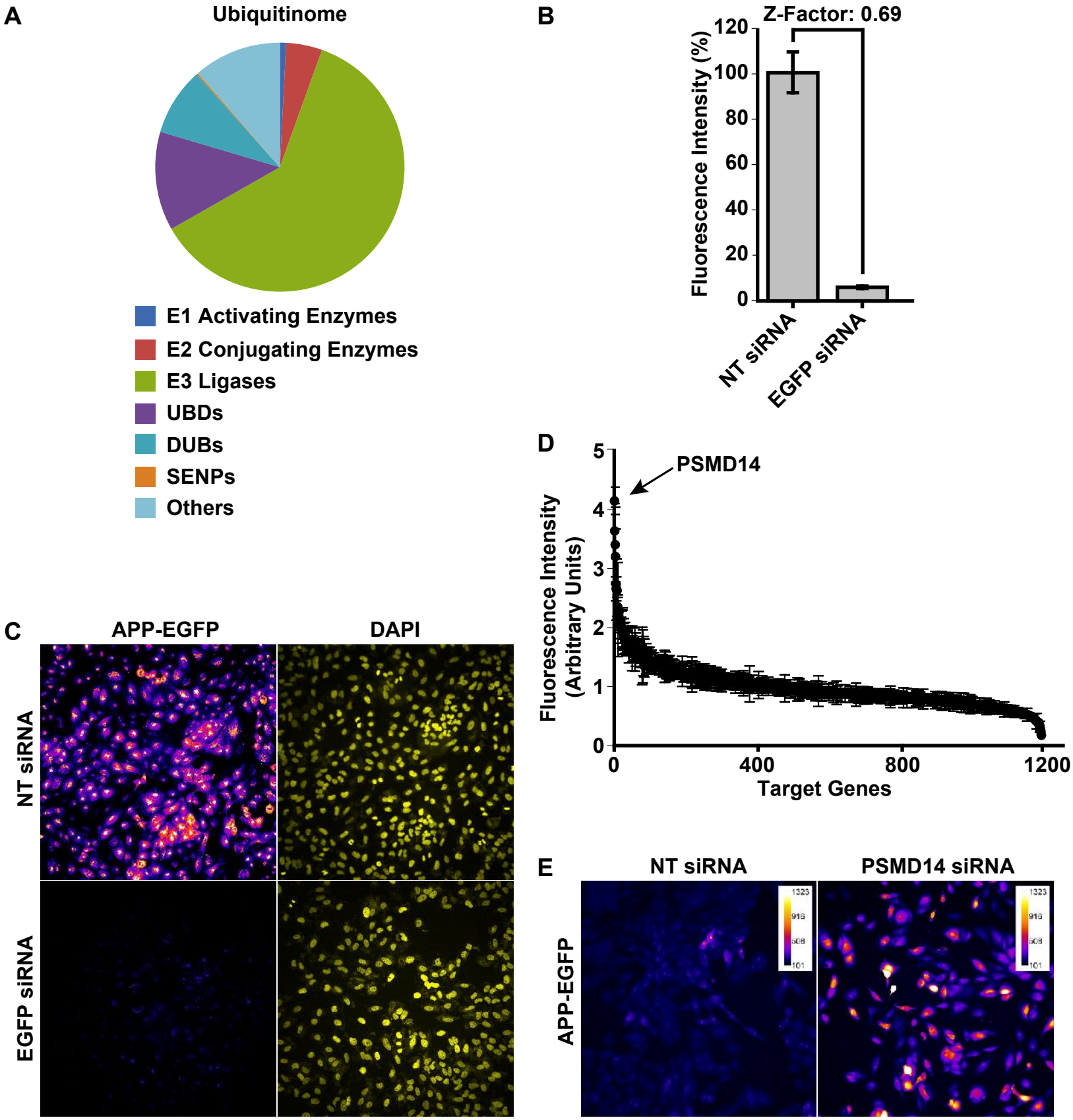
A
Ubiquitinome
E1 Activating Enzymes
E2 Conjugating Enzymes
E3 Ligases
UBDs
DUBs
SENPs
Others
B
Z-Factor: 0.69
Fluorescence Intensity (%)
120
100
80
60
40
20
0
NT siRNA
EGFP siRNA
C
APP-EGFP
DAPI
NT siRNA
EGFP siRNA
D
PSMD14
Fluorescence Intensity
(Arbitrary Units)
5
4
3
2
1
0
0
400
800
1200
Target Genes
E
NT siRNA
PSMD14 siRNA
APP-EGFP

**Figure 1**

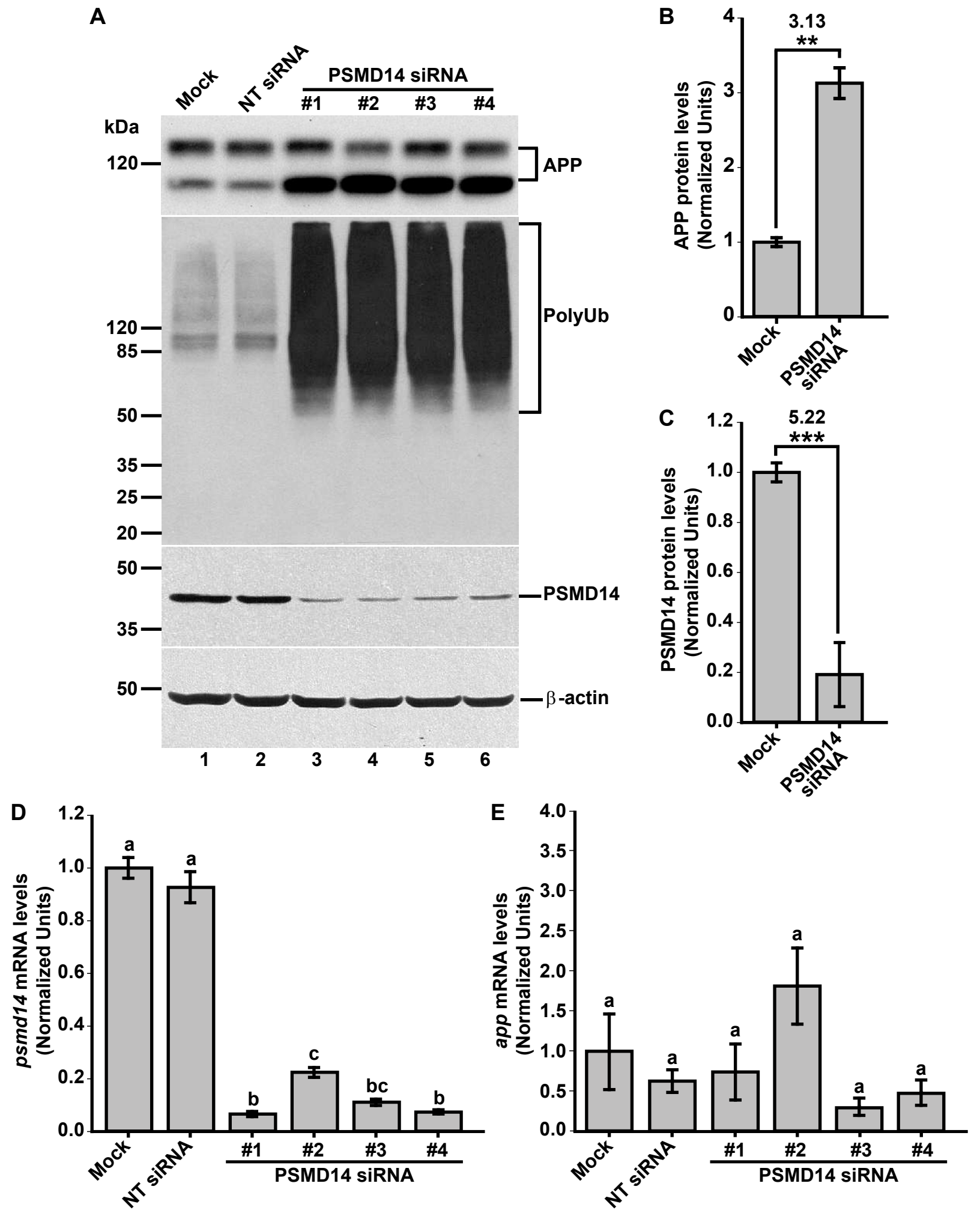
A
Mock
NT siRNA
PSMD14 siRNA
#1
#2
#3
#4
kDa
120
APP
120
85
50
35
25
20
PolyUb
50
35
PSMD14
50
β-actin
1
2
3
4
5
6
B
3.13
**
APP protein levels (Normalized Units)
Mock
PSMD14 siRNA
C
5.22
***
PSMD14 protein levels (Normalized Units)
Mock
PSMD14 siRNA
D
psmd14 mRNA levels (Normalized Units)
a
a
b
c
bc
b
Mock
NT siRNA
#1
#2
#3
#4
PSMD14 siRNA
E
app mRNA levels (Normalized Units)
a
a
a
a
a
a
Mock
NT siRNA
#1
#2
#3
#4
PSMD14 siRNA

**Figure 2**

119 1 and 2, respectively). Quantification analysis showed a 3.13-fold increase of full-length
120 endogenous APP levels in PSMD14 KD cells, compared to Mock cells (Fig. 2B). Besides,
121 we found that silencing of PSMD14 caused a strong increase in high molecular weight Ub
122 conjugates, consistent with the role of PSMD14 as a proteasomal subunit with DUB
123 activity (Fig. 2A, second panel, lanes 3-6 compared to lanes 1 and 2). Confirmation of the
124 efficient KD of PSMD14 with all four siRNAs tested was demonstrated by western blot
125 (Fig. 2A, third panel, lanes 3-6 compared to lanes 1 and 2), observing a 5.22-fold decrease
126 on PSMD14 levels (Fig. 2C). Moreover, efficient KD of PSMD14 was also determined by
127 quantitative reverse transcription PCR (RT-qPCR) (Fig. 2D). Finally, to evaluate whether
128 the increase of APP protein levels in PSMD14 KD cells could be the result of an up-
129 regulation of APP transcription, we evaluated *APP* mRNA levels by RT-qPCR, observing
130 no significant changes (Fig. 2E). Altogether, these findings indicate that the silencing of
131 PSDM14 caused a robust increase of APP protein levels, a finding that could suggests
132 impairment in its turnover due to trafficking alterations.

133 ***Acute inhibition of the deubiquitinating enzyme PSMD14 of the 19S RP accumulates***
134 ***APP in a swollen Golgi apparatus.***

135 To determine whether PSMD14 is involved in the control of endogenous APP levels, we
136 investigated the effect of incubating cells with Capzimin (CZM), a potent and specific
137 inhibitor of the DUB activity of PSMD14[37], a subunit of the 19S RP of the proteasome
138 (Fig. 3A). We observed that CZM led to a significant increment in full-length endogenous
139 APP levels in a dose-dependent manner, compared to untreated cells (Fig. 3B and 3C).
140 Interestingly, compared to untreated cells, and in contrast to CZM, treatment with a
141 standard concentration of 10 μM MG132, a reversible inhibitor of the β1, β2 and β5
142 subunits of the 20S catalytic core of the proteasome[38,39] (Fig. 3A), caused a significant
143 decrease in full-length endogenous APP levels (Fig. 3B and 3C). To confirm the inhibition
144 of PSMD14 by CZM, we tested the effect of this inhibitor on the levels of high molecular
145 weight Ub conjugates, comparing it with MG132. In agreement with the effect of PSMD14
146 KD, we observed that CZM caused a robust increase in high molecular weight Ub
147 conjugates in a dose-dependent manner, finding a maximum effect with 10 μM CZM (Fig.
148 3D). However, we noticed that 10 μM MG132 caused a more powerful increase in Ub
149 conjugates (Fig. 3D). To confirm the accumulation of Ub conjugates by these treatments,

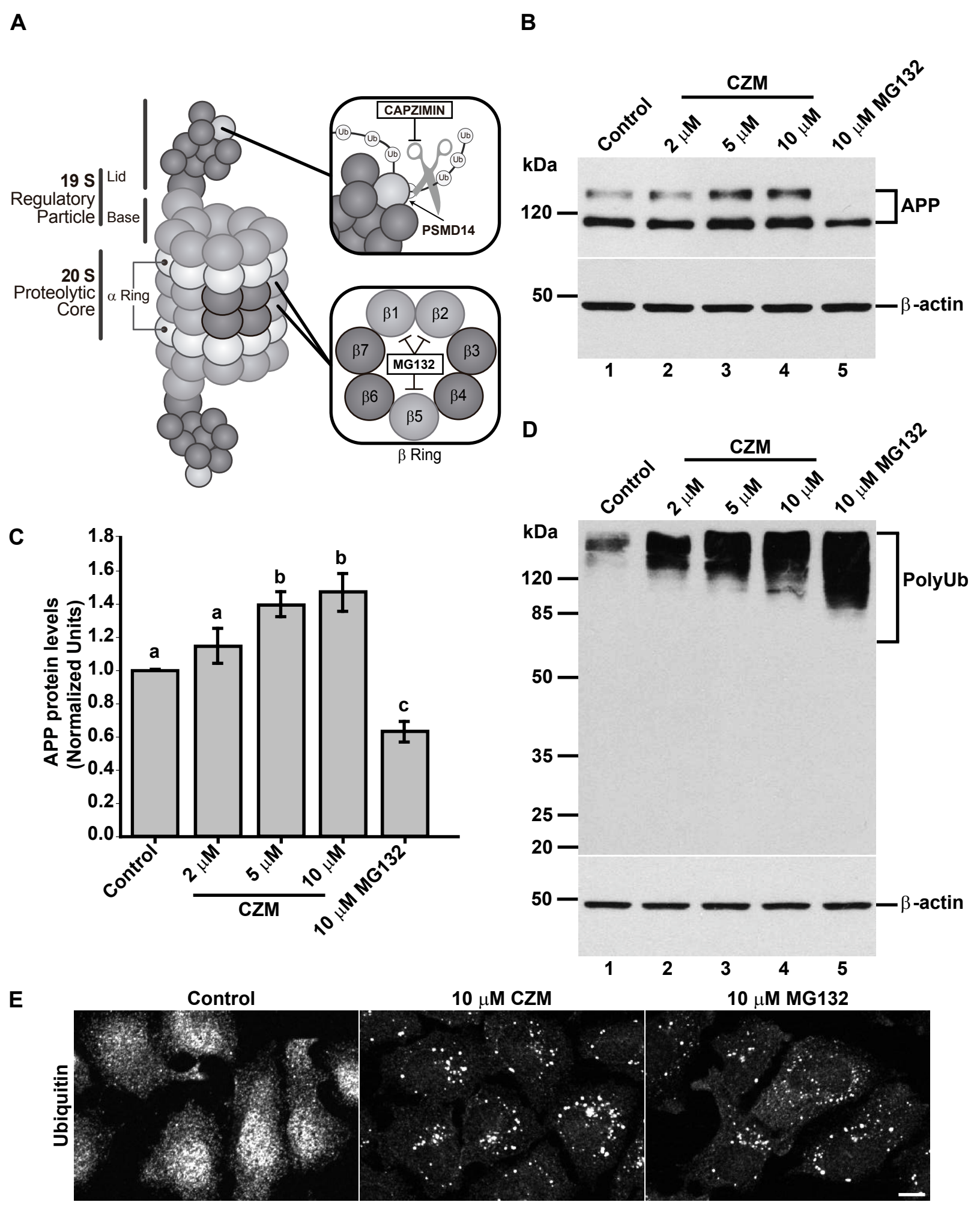
A
19 S Regulatory Particle
Lid
Base
20 S Proteolytic Core
α Ring
CAPZIMIN
Ub
PSMD14
β1
β2
β3
β4
β5
β6
β7
MG132
β Ring
B
CZM
Control
2 μM
5 μM
10 μM
10 μM MG132
kDa
120
50
APP
β-actin
1
2
3
4
5
C
APP protein levels (Normalized Units)
1.8
1.6
1.4
1.2
1.0
0.8
0.6
0.4
0.2
0.0
a
a
b
b
c
Control
2 μM
5 μM
10 μM
10 μM MG132
CZM
D
CZM
Control
2 μM
5 μM
10 μM
10 μM MG132
kDa
120
85
50
35
25
20
50
PolyUb
β-actin
1
2
3
4
5
E
Control
10 μM CZM
10 μM MG132
Ubiquitin

**Figure 3**

150 we studied the presence of Ub-inclusion bodies by immunofluorescence analysis. We found
151 that, compared to untreated cells (Fig. 3E, left panel), 10 μM CZM (Fig. 3E, middle panel)
152 caused a similar accumulation of cytoplasmic Ub-inclusion bodies than 10 μM MG132
153 (Fig. 3E, right panel). Together, our results confirm that acute inhibition of PSMD14 by
154 CZM replicates the phenotype obtained by PSMD14 KD regarding to the impact on the
155 endogenous APP levels. Thus, CZM offers a pharmacological tool to address whether the
156 activity of PSDM14 is required for APP membrane trafficking.
157 To unveil this possibility, we performed an immunofluorescence analysis of endogenous
158 APP in parental H4 cells. We observed that the treatment with 10 μM CZM resulted in a
159 perinuclear redistribution of APP, which is highly indicative of Golgi apparatus localization
160 (Fig. 4D, compared to 4A). Moreover, similar to the PSMD14 KD, we observed that the
161 CZM treatment caused a significant 2.50-fold increase in APP total fluorescence intensity
162 compared to untreated cells (Fig. 4G). We also observed a significant 1.92-fold increase in
163 the amount of APP in the area positive to the Golgi matrix protein GM130 (GM130),
164 compared to the total area (Fig. 4F, compared to 4C and Fig. 4H). Moreover, we observed
165 that the treatment with CZM caused a significant 1.30-fold increase in the total cell area
166 (Fig. 4I). In addition, we found that CZM caused the swelling of the Golgi apparatus (Fig.
167 4E compared to 4B), a phenotype that is shown in a zoom in Fig. 4J. To confirm this
168 phenotype, we performed measurements of GM130 images from confocal 3D
169 reconstructions from the Z-stacks of cells treated with CZM (Fig. 4K). We observed a 1.53-
170 fold increase in the Golgi apparatus volume in CZM treated cells, compared to control cells
171 (Fig. 4L). Similar results were observed in quantitative 2D image analysis, observing a
172 significant 2.53-fold increase in the Golgi apparatus area upon CZM treatment (Suppl. Fig.
173 1). Altogether, our results show that acute inhibition of PSMD14 by CZM accumulates
174 APP in a swollen Golgi apparatus. These findings strongly suggest that CZM impairs the
175 Golgi apparatus due to perturbations of the trafficking through this organelle.
176 ***Acute inhibition of the deubiquitinating enzyme PSMD14 perturbs Golgi-to-ER***
177 ***retrograde transport***
178 The Golgi apparatus is a highly dynamic organelle that requires fine regulation of
179 trafficking pathways in order to maintain its size, shape and composition. In particular, it
180 has been shown that Golgi-to-ER retrograde transport plays a crucial role in the

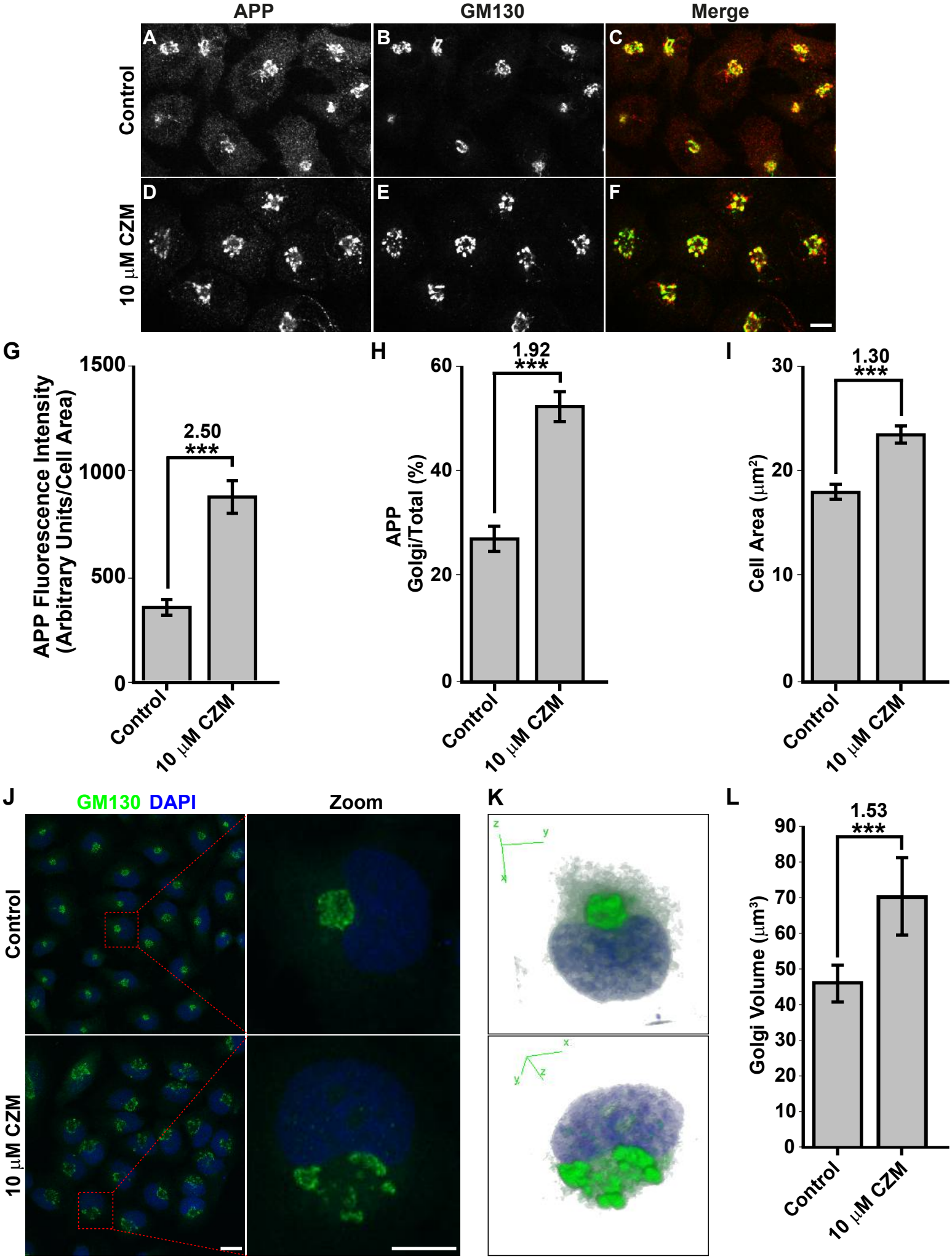
APP
GM130
Merge
A
B
C
D
E
F
Control
10 μM CZM
G
APP Fluorescence Intensity (Arbitrary Units/Cell Area)
1500
1000
500
0
2.50
***
Control
10 μM CZM
H
APP Golgi/Total (%)
60
40
20
0
1.92
***
Control
10 μM CZM
I
Cell Area (μm²)
30
20
10
0
1.30
***
Control
10 μM CZM
J
GM130 DAPI
Zoom
Control
10 μM CZM
K
L
Golgi Volume (μm³)
90
80
70
60
50
40
30
20
10
0
1.53
***
Control
10 μM CZM

Figure 4

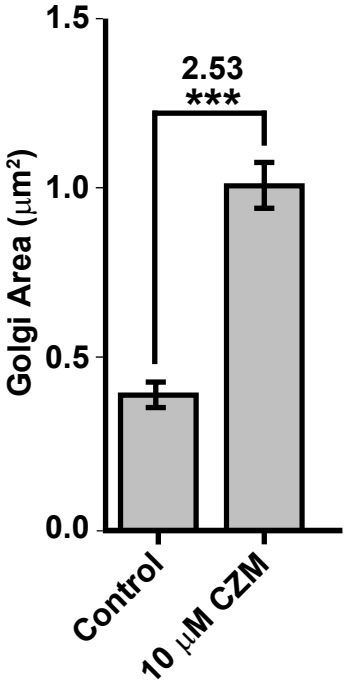


**Supplementary Figure 1**

181 maintenance of Golgi morphology. Indeed, inhibition of this specific trafficking pathway
182 results in a significant swelling of this organelle [40–45]. To investigate whether the swelling
183 of the Golgi by the inhibition of PSMD14 with CZM could be the result of the inhibition of
184 the Golgi-to-ER retrograde transport, we first validated our findings in HeLa cells. We
185 measured Golgi apparatus volume in 3D reconstructions from the Z-stacks of untreated
186 HeLa cells or treated with CZM and MG132 by using Giantin as Golgi apparatus reporter.
187 Similar to our findings in H4 cells, we found that the inhibition of PSMD14 DUB activity
188 by CZM causes a 2.14-fold increase in Golgi apparatus volume (Fig. 5A, middle panel
189 compared to the left panel and 5B). Interestingly, in contrast to CZM, we observed that
190 MG132 caused no effect on Golgi apparatus volume (Fig. 5A, right panel compared to the
191 left panel and 5B), strongly suggesting that Golgi homeostasis is regulated by the PSMD14
192 DUB activity. Then, we investigated whether this phenotype was the result of Golgi-to-ER
193 retrograde transport inhibition. We assessed the distribution of stably overexpressed KDEL
194 (Lys-Asp-Glu-Leu) Receptor 1 (KDELR1) fused to GFP (KDELR1-GFP) in HeLa cells.
195 As it was previously reported [44,46], overexpressed KDELR1-GFP is mostly distributed to
196 the ER due to its efficient transport from the Golgi apparatus to the ER (Fig. 5C, left panel
197 and 5D). Thus, impairment of Golgi-to-ER retrograde transport causes the accumulation of
198 KDELR1-GFP in the Golgi apparatus working as an assay to identify novel regulators of
199 this pathway [44]. Interestingly, we found that CZM caused a rapid time-dependent
200 accumulation of KDELR1-GFP at the Golgi apparatus, observing a maximal effect after 90
201 min of treatment (Suppl. Fig. 2). At this time, we observed a significant 1.50-fold increase
202 in the amount of KDELR1-GFP within the Giantin-positive Golgi apparatus, compared to
203 the total area (Fig. 5C, middle panel compared to the left panel, and 5D). As before, we
204 tested the effect of MG132, observing no effect on the distribution of KDELR1-GFP (Fig
205 5C, right panel compared to left panel, and 5D), which strongly supports that MG132 has
206 no effect on Golgi-to-ER retrograde transport. Next, to confirm blockage of Golgi-to-ER
207 retrograde transport by the acute inhibition of the PSMD14, we tracked the redistribution of
208 the transiently overexpressed thermo-sensitive KDELR1-VSVG-YFP chimera (vesicular
209 stomatitis virus G protein fused to KDEL receptor 1 and YFP) in HeLa cells upon treatment
210 with CZM by live cell imaging at different temperatures. Briefly, at a permissive
211 temperature of 32°C, KDELR1-VSVG-YFP cycles between the Golgi apparatus and the

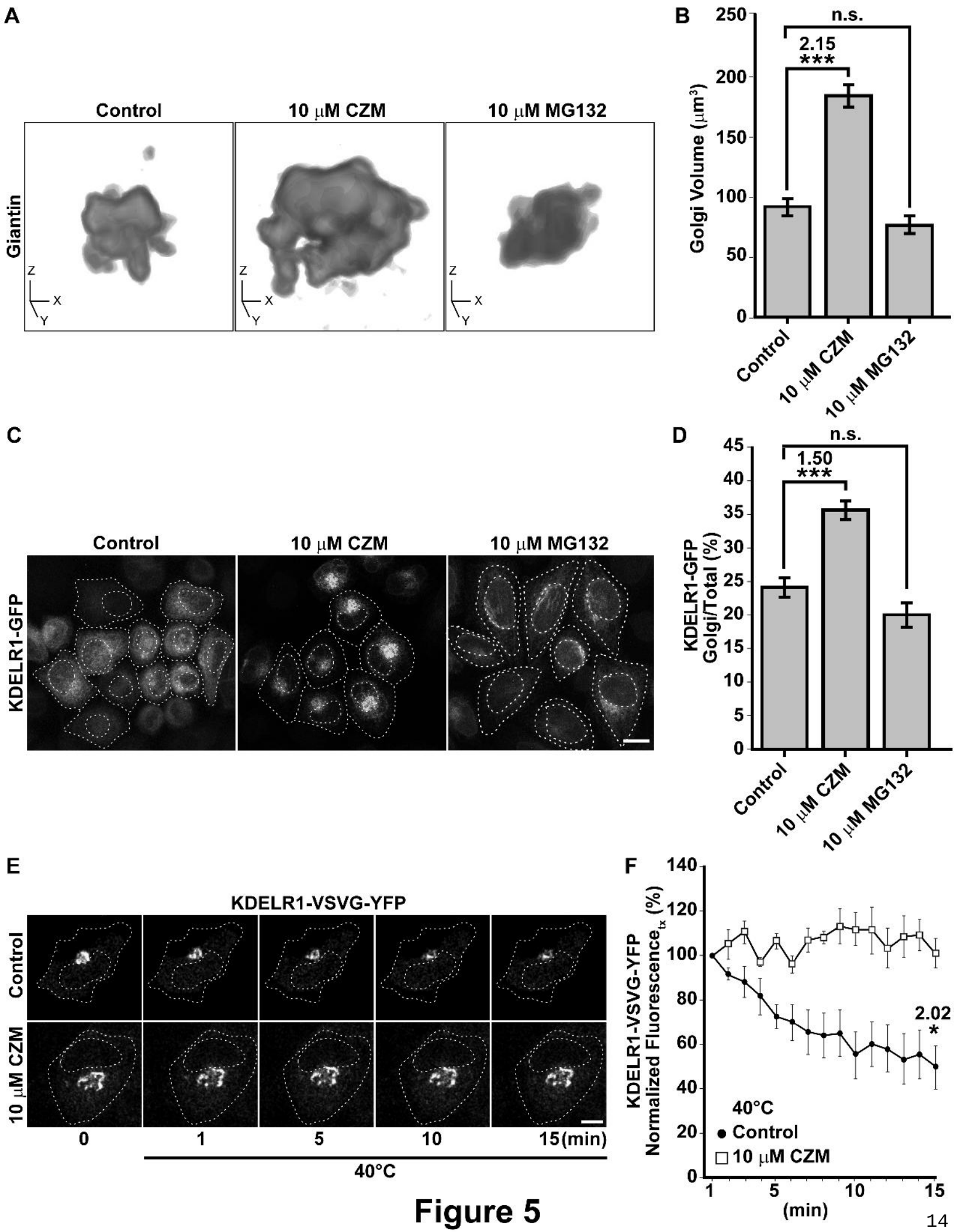
A
Control
10 μM CZM
10 μM MG132
Giantin
Z
X
Y
B
n.s.
2.15
***
Golgi Volume (μm³)
250
200
150
100
50
0
Control
10 μM CZM
10 μM MG132
C
Control
10 μM CZM
10 μM MG132
KDELR1-GFP
D
n.s.
1.50
***
KDELR1-GFP Golgi/Total (%)
45
40
35
30
25
20
15
10
5
0
Control
10 μM CZM
10 μM MG132
E
KDELR1-VSVG-YFP
Control
10 μM CZM
0
1
5
10
15(min)
40°C
F
KDELR1-VSVG-YFP Normalized Fluorescence$_{tx}$ (%)
140
120
100
80
60
40
20
0
2.02
*
40°C
Control
10 μM CZM
1
5
10
15
(min)

Figure 5

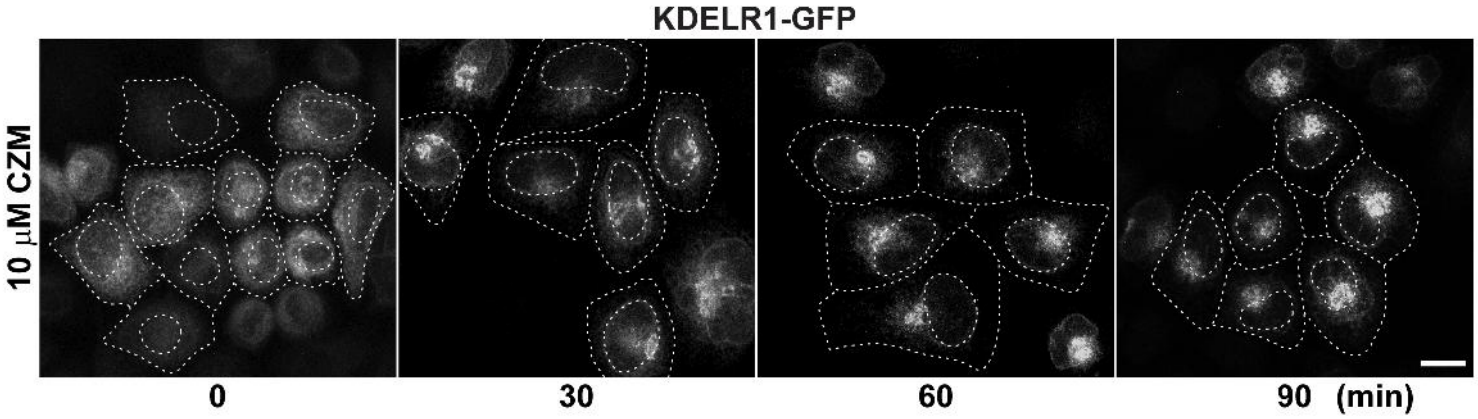


**Supplementary Figure 2**

212 ER, showing distribution mainly at the Golgi apparatus. Upon shifting to a restrictive
213 temperature of 40°C, KDELR1-VSVG-YFP is progressively accumulated at the ER due to
214 its specific retention in this compartment at this temperature. In addition, because the
215 Golgi-to-ER retrograde transport is not affected at 40ºC, the rapid decay of the fluorescence
216 of KDELR1-VSVG-YFP fluorescence at the Golgi apparatus, a measurement that is used to
217 evaluate inhibition of Golgi-to-ER retrograde transport pathway [47]. We found that in
218 control cells nearly 50% of the fluorescence of KDELR1-VSVG-YFP decayed after 15 min
219 of shifting the temperature to 40°C (Fig. 5E, upper panels and 5F), indicating that
220 retrograde transport is working normally [47]. In contrast, when cells were treated with CZM,
221 the decay of the fluorescence of KDELR1-VSVG-YFP was not apparent, confirming that
222 acute inhibition of the PSMD14 blocked Golgi-to-ER retrograde transport (Fig. 5E, lower
223 panels and 5F). In contrast, MG132 treated cells showed similar results as controls (data not
224 shown), confirming that the 20S proteasome has no effect on retrograde transport.
225 Importantly, we found that CZM is able to block retrograde transport for short times having
226 no effect on the catalytic activity of the 20S proteasome (Suppl. Fig. 3). In contrast, a rapid
227 and robust inhibition on the catalytic activity of the 20S proteasome is observed with
228 MG132 (Suppl. Fig. 3). These findings strongly indicate that acute inhibition of PSMD14
229 DUB activity by CZM acts as a powerful blocker of Golgi-to-ER retrograde transport,
230 explaining the swelling of the Golgi apparatus and the accumulation of protein cargoes
231 such as APP at this location.

232 ***Inhibition of Golgi-to-ER retrograde transport by CZM has a negative impact on***
233 ***macroautophagy.***

234 Several lines of evidence have shown that Golgi-to-ER retrograde transport plays a relevant
235 role in autophagosome biogenesis at the level of the ER [48–51]. In addition, it has been shown
236 that PSMD14 participates in the activation of the aggresome clearance by cleaving K63 Ub
237 chains of aggregate proteins[52,53]. Thus, we investigated the effect of acute inhibition of
238 PSMD14 DUB activity on the number of autophagosomes by testing the classical marker
239 microtubule-associated protein 1 light chain 3B (LC3B) [54]. Therefore, parental H4 cells were
240 treated under nutrient starvation with Earle's balanced salt solution (EBSS), an established
241 culture medium used for activation of autophagosomal formation [55]. As expected, we found
242 that starvation strongly increased the number of autophagosomes (Fig. 6B), compared to

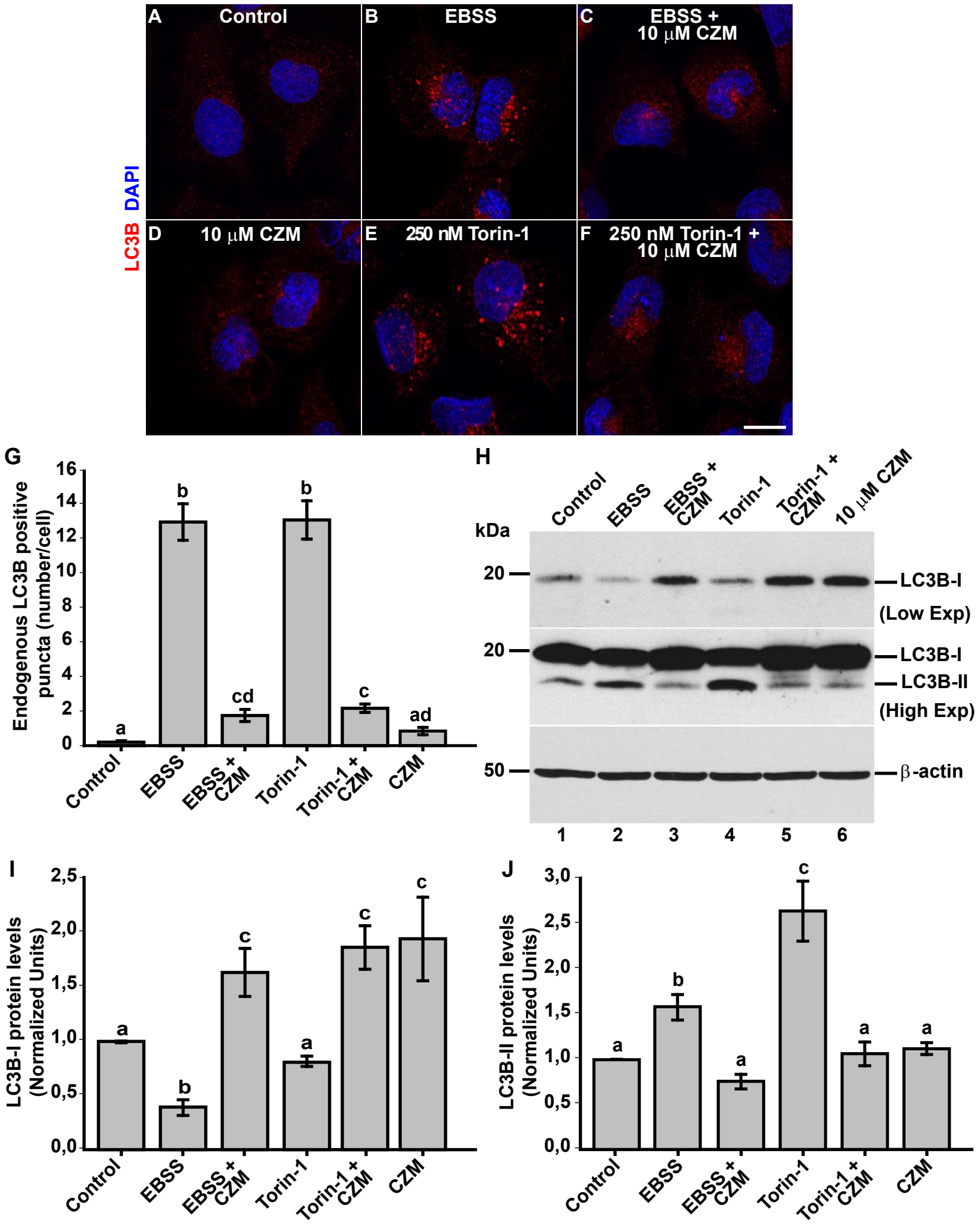
A Control
B EBSS
C EBSS + 10 μM CZM
D 10 μM CZM
E 250 nM Torin-1
F 250 nM Torin-1 + 10 μM CZM
DAPI
LC3B
G
Endogenous LC3B positive puncta (number/cell)
Control
EBSS
EBSS + CZM
Torin-1
Torin-1 + CZM
CZM
H
kDa
LC3B-I (Low Exp)
LC3B-I
LC3B-II (High Exp)
β-actin
I
LC3B-I protein levels (Normalized Units)
J
LC3B-II protein levels (Normalized Units)

**Figure 6**

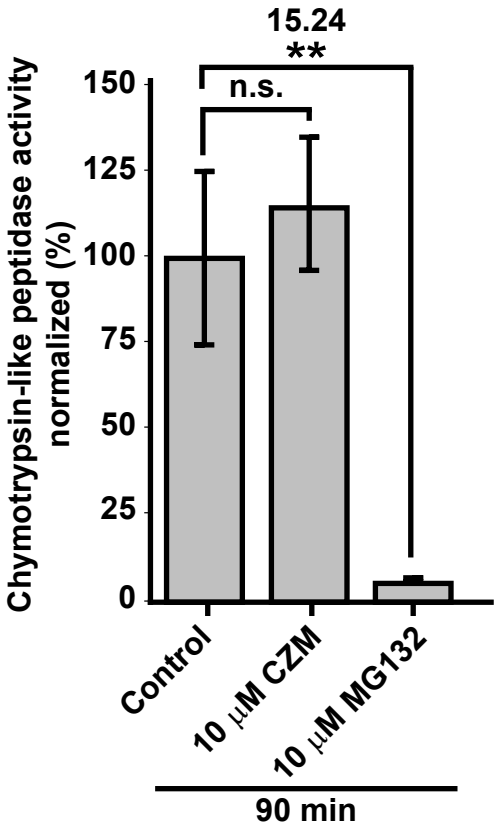


**Supplementary Figure 3**

243 cells treated under normal nutrient conditions (Fig. 6A). In contrast, we observed that
244 treatment with CZM abolished the appearance of autophagosomes upon EBSS treatment
245 (Fig. 6C compared to 6B). We also tested the effect of CZM in cells under normal nutrients
246 conditions, but in the absence or presence of Torin-1, a potent and selective inhibitor of
247 mammalian target of rapamycin complexes (mTORC1/2), a trigger of autophagosomal
248 formation[56]. Similar to the results with EBSS, we observed that CZM prevented the
249 appearance of autophagosomes promoted by Torin-1 (Fig. 6F compared to 6E). In
250 agreement with these findings, we observed that CZM alone did not increase the number of
251 autophagosomes (Fig. 6D compared to 6A), in contrast to the effect of MG132 (Suppl. Fig.
252 4). To confirm these results, we quantified the number of LC3-positive structures under all
253 conditions tested, observing a significant decrease in the number of autophagosomes when
254 cells, treated with EBSS solution or Torin-1, where also treated with CZM (Fig. 6G). In
255 addition, we validated these results biochemically performing western blot analysis of
256 endogenous LC3B (Fig. 6H). We found that the levels of LC3B-II were strongly increased
257 with EBSS or Torin-1 treatment (Fig. 6H, lanes 2 and 4). In contrast, when cells were
258 treated with EBSS or Torin-1 in the presence of CZM, LC3B-II levels did not change (Fig.
259 6H, lanes 3 and 5) compared to control cells (Fig. 6H, lane 1), results that were quantified
260 and depicted in Fig. 6J. Interestingly, this biochemical analysis also showed that CZM
261 increased LC3B-I levels under all conditions tested (Fig. 6H, lanes 3, 5 and 6, and Fig. 6I)
262 compared to control cells (Fig. 6H, lane 1), suggesting that the reduction of the
263 autophagosomal structures caused by CZM was not due to a reduction in LC3B total levels.
264 Altogether, these results confirm that acute inhibition of PSMD14 DUB activity acts as a
265 potent blocker of autophagosome biogenesis induced by EBSS or Torin-1. In addition,
266 these findings suggest that blockage of autophagosomal biogenesis could be a consequence
267 of Golgi-to-ER retrograde transport inhibition.

268 ***Inhibition of Golgi-to-ER retrograde transport by CZM accumulates RAB1A and***
269 ***ATG9A at the Golgi apparatus***

270 To evaluate this hypothesis, we tested the effect of acute inhibition of the PSMD14 DUB
271 activity on the distribution of proteins implicated in the initial steps of autophagosome
272 formation, which traffics in early compartments of the secretory pathway. We first tested
273 RAB1A, a small GTPase with an essential role in the initiation of autophagy, facilitating

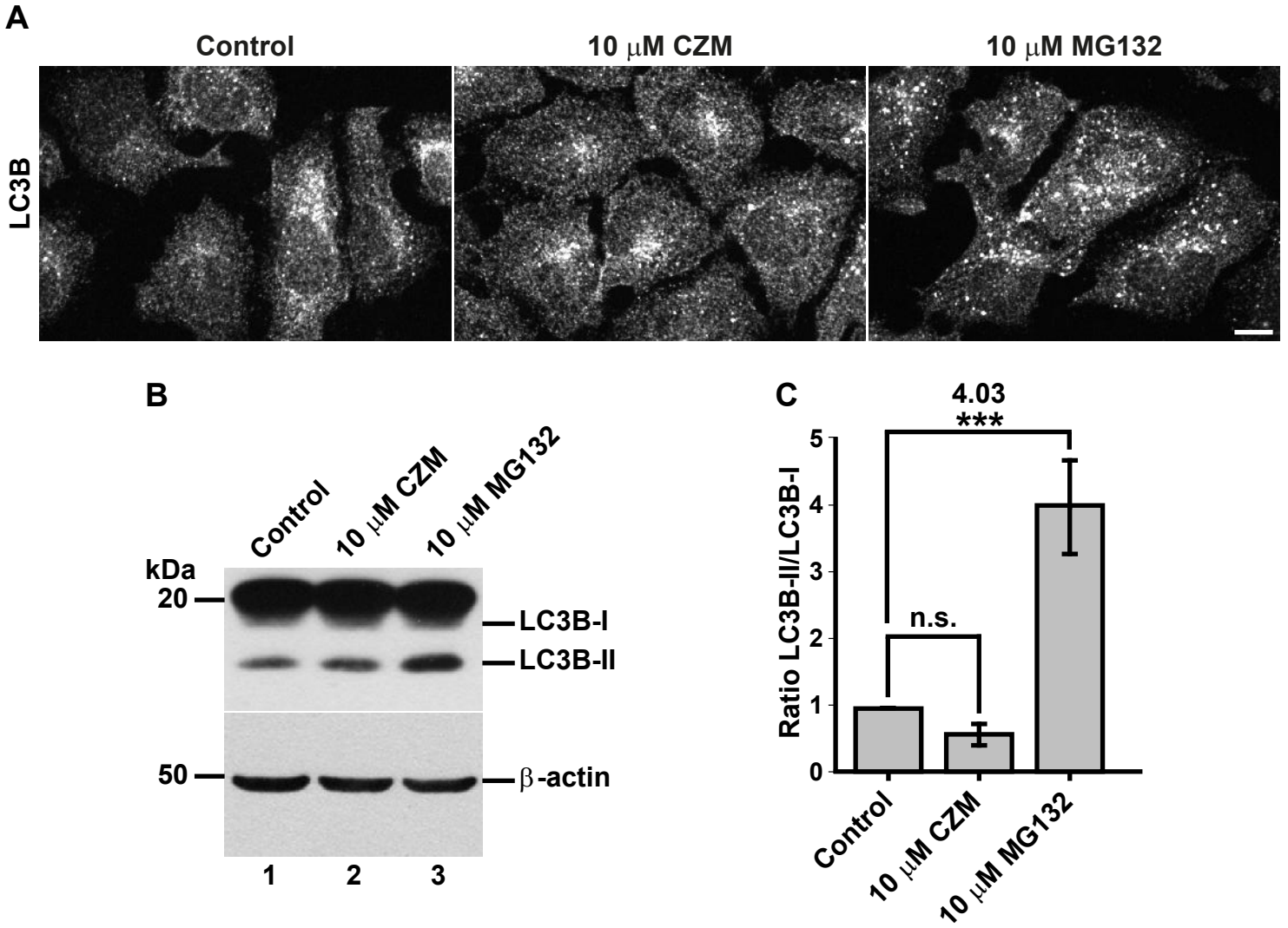


# Supplementary Figure 4

274 the recruitment of the unc-51-like kinase 1 (ULK1) complex to subdomains of the ER, a
275 crucial early step during autophagosome formation [57,58]. We found that CZM treatment
276 caused a redistribution of RAB1A to the perinuclear zone (Fig. 7A). Measuring these
277 images confirmed a significant increase of RAB1A in this area (Fig. 7B), a result that was
278 accompanied by a decrease of RAB1A in the cell periphery defined as radial zone (Fig.
279 7B). Importantly, we found that RAB1B was not affected by the same condition (data not
280 shown). Moreover, we observed that RAB1A was distributed in the swollen Golgi
281 apparatus, similar to GM130, upon CZM treatment (Suppl. Fig. 5). With the same aim, we
282 studied the distribution of ATG9A, an essential transmembrane protein involved in
283 macroautophagy, which plays a crucial role in the early steps of autophagosome formation
284 [59,60]. ATG9A-containing vesicles are formed from the Golgi apparatus translocating to the
285 ER to form the initiation site at the ER for autophagosome formation [61]. Similar to RAB1A,
286 we found that acute inhibition of PSMD14 caused a redistribution of ATG9A to the
287 perinuclear zone, together with a decrease in its distribution in the radial zone (Fig. 7C).
288 The quantification analysis of these images is shown in Fig. 7C. Moreover, and similar to
289 RAB1A, we observed that ATG9A is distributed to the swollen GM130-Golgi apparatus
290 area upon CZM treatment (Suppl. Fig. 6). These results strongly indicate that blockage of
291 Golgi-to-ER retrograde transport by acute inhibition of PSMD14 DUB activity causes the
292 retention at the Golgi apparatus of key proteins implicated in early steps of autophagosome
293 formation. The PSDM14-dependent inhibition of autophagy explains the accumulation of
294 APP at the Golgi apparatus since macroautophagy has been recently demonstrated as a
295 positive regulator of protein secretion from the Golgi apparatus[62]. Collectively, these results
296 show the strong interplay between membrane transport and autophagy through a novel
297 mechanism involving the proteasome complex through the deubiquitinating activity of
298 PSMD14.

299 **Discussion**

300 We report here that PSMD14 DUB activity, a subunit of the 19S RP of the proteasome,
301 functions as a novel regulator of autophagosome formation. To our knowledge, this is the
302 first report demonstrating that impairment of the proteasome can have a negative impact on
303 the initiation of autophagy. Several reports have shown that inhibition of the 20S catalytic

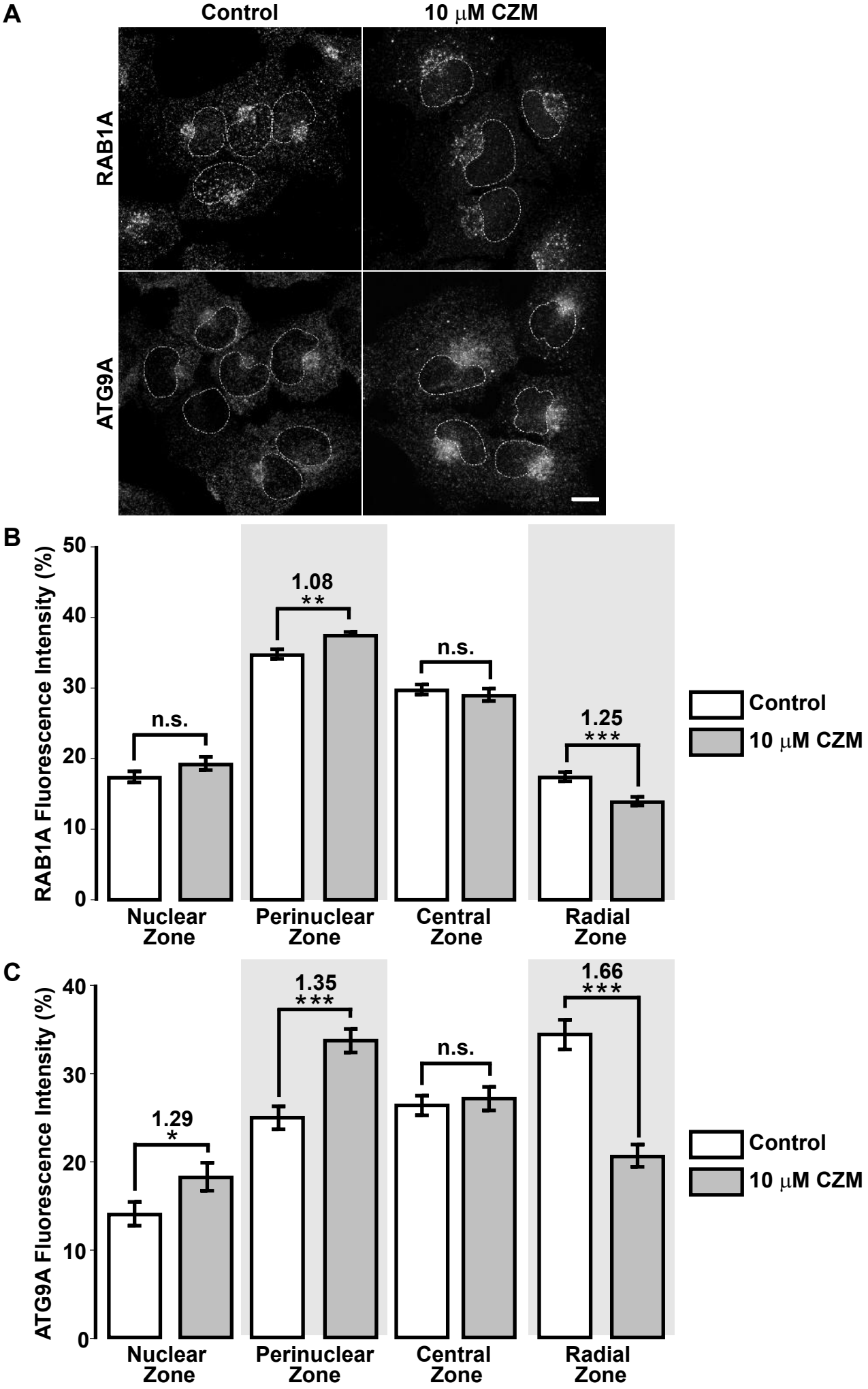
A
Control
10 μM CZM
RAB1A
ATG9A
B
RAB1A Fluorescence Intensity (%)
50
40
30
20
10
0
n.s.
1.08
**
n.s.
1.25
***
Nuclear Zone
Perinuclear Zone
Central Zone
Radial Zone
Control
10 μM CZM
C
ATG9A Fluorescence Intensity (%)
40
30
20
10
0
1.29
*
1.35
***
n.s.
1.66
***
Nuclear Zone
Perinuclear Zone
Central Zone
Radial Zone
Control
10 μM CZM

**Figure 7**

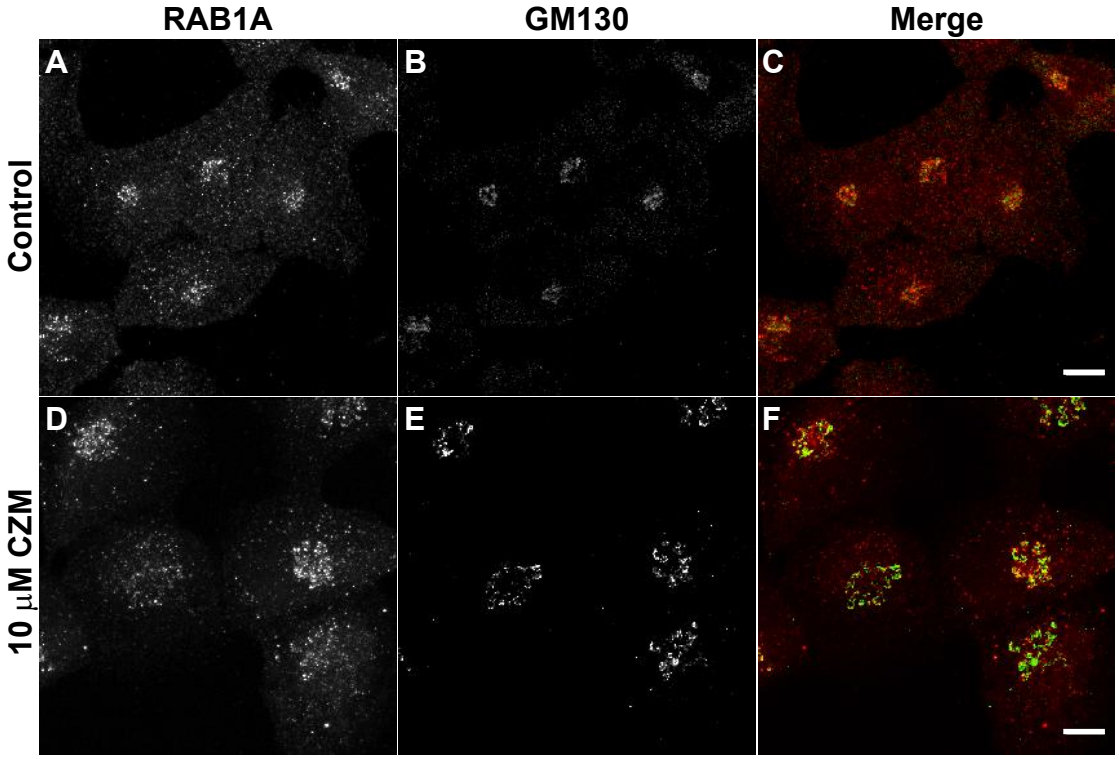


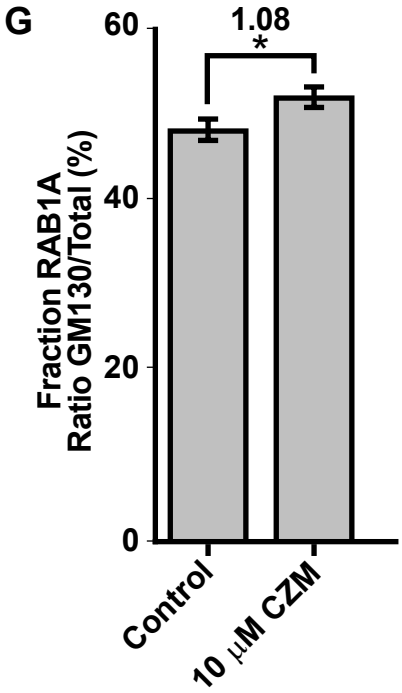


# Supplementary Figure 5

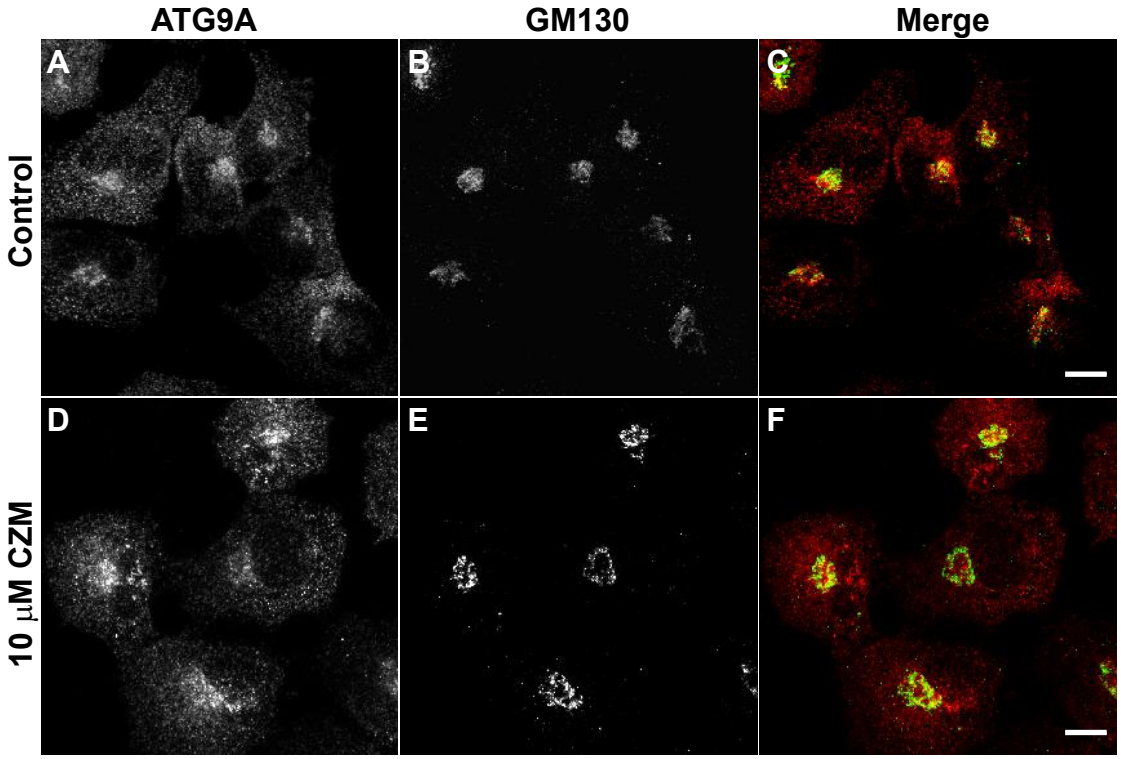


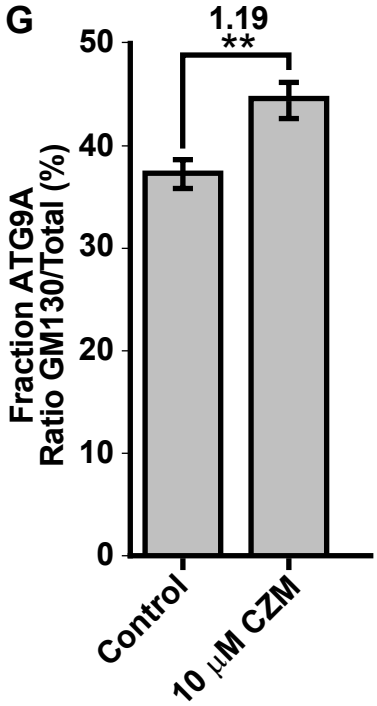


# Supplementary Figure 6

304 core of the proteasome by blockers of the β-subunits trigger the enhancement of the
305 biogenesis of LC3B-positive autophagosomes [63–68]. Contrary to these findings, we found
306 that the blockage of the PSMD14 DUB activity perturbs the biogenesis of LC3B-positive
307 autophagosomes. Because the inhibition of PSMD14 DUB activity but not the blockage of
308 the 20S catalytic core blocked Golgi-to-ER retrograde transport, a pathway implicated in
309 the initiation of autophagosomes [48–51], we postulated that PSMD14 DUB activity controls
310 autophagy by a process independent of bulk proteasomal degradation but dependent on
311 K63-Ub chains. Indeed, K63-Ub chains has been directly involved in the recycling of
312 transmembrane cargoes into the endosomal pathway in *C. elegans*[69]. In addition, K63-Ub
313 chains regulate positively autophagy by mTORC inactivation through K63-linked
314 polyubiquitination of RagA[70], and by promoting K63-chain autoubiquitination of the E3
315 ligase TRIM13 that increases the interaction with the autophagy receptor p62 promoting
316 initiation of ER-phagy[71]. Likewise, the deconjugation of K63-Ub chains has biological
317 relevance. Free unanchored K63-Ub chains release in a PSMD14 dependent manner are
318 crucial to coordinate the elimination of protein aggregates by autophagy[52]. Free unanchored
319 K63-Ub chains bind and activate the deacetylase HDAC6[52,53], which contributes to relocate
320 the aggregates to the aggresome for final autophagic clearence[72-83]. Here, we unveil the first
321 insight into the regulation of Golgi-to-ER retrograde transport by K63-Ub chains by the
322 functional role of the deubiquitinating enzyme PSMD14. We hypothesize that the function
323 of key cytosolic proteins implicated in Golgi-to-ER retrograde transport are under the
324 control of K63-Ub chains, confirming the crucial regulatory role of deubiquitination in
325 membrane protein trafficking [73,74].
326 In this regard, key regulatory proteins involved in Golgi-to-ER transport are regulated by
327 the state of ubiquitination/deubiquitination. In yeast, deletion of the DUB Ube3p and its co-
328 factor Bre5p accumulates ubiquitinated β′-COP facilitating its rapid degradation by the
329 proteasome [75,73]. Because β′-COP is a subunit of the COP-I coatomer complex, a key
330 machinery implicated in Golgi-to-ER retrograde transport, reduction in β′-COP levels
331 perturbs this trafficking pathway [73]. Two other proteins that participates in this retrograde
332 trafficking pathway, such as PKA and UVRAG [44,76], have been shown to be regulated by
333 ubiquitination. Blockers of PKA signaling cause inhibition of this trafficking pathway, a
334 process that is accompanied by the swelling of the Golgi apparatus [44,45]. It has been shown

335 that the catalytic PKA subunit (PKAc) is ubiquitinated by the CHIP E3 ligase, resulting in
336 proteasomal degradation of PKAc and signaling shutdown [77]. UVRAG mediates the
337 interaction of β′-COP with ER tethers and COP-I coatomer for efficient fusion of
338 retrograde vesicles to the ER, a crucial step during Golgi-to-ER retrograde transport [49].
339 UVRAG is ubiquitinated by SMURF1 [78] and its silencing causes the swelling of the Golgi
340 apparatus and the inhibition of the Golgi-to-ER retrograde transport [49]. Whether these
341 proteins are regulated by K63-Ub chains is unknown and should be further addressed.
342 In addition, we propose that Golgi-to ER retrograde transport inhibition by PSMD14
343 dysfunction might result on the accumulation of structural and/or autophagy regulatory
344 elements. In fact, the inhibition of PSMD14 caused the accumulation of ATG9A at the
345 Golgi. ATG9A is a multispanning membrane protein essential for autophagy [59,60]. ATG9A
346 is actively transported through Golgi-to-ER retrograde transport [61] and participates as a key
347 player in the biogenesis of autophagosomes [59,79]. Moreover, along with the accumulation of
348 ATG9A at the Golgi, we found increased levels of RAB1A at the Golgi apparatus. RAB1A
349 is an essential small GTPase that participates in the recruitment of the ULK1 complex to
350 subdomains of the ER for autophagy initiation [57,58]. Interestingly, and similar to PSMD14
351 inhibition, ATG9A deficiency causes an increase in LC3B-I levels, accompanied by a
352 reduction in the number of autophagosome structures [59,79,80]. Together, our results strongly
353 support that PSMD14 inhibition perturbs autophagosome biogenesis due to the
354 sequestration of key proteins of this process at the Golgi apparatus. In addition, it supports
355 the hypothesis of a closed intersection between Golgi-to-ER retrograde and autophagy
356 pathway [49,76] whereas PSMD14 DUB activity emerged as a new regulatory element of this
357 intersection. The PSDM14-dependent inhibition of macroautophagy might affect protein
358 secretion from the Golgi apparatus since autophagy has been recently demonstrated as a
359 positive regulator of this process[62] as observed by the strong accumulation of APP at the
360 Golgi apparatus. Collectively, the results demonstrate the strong functional interplay
361 between membrane transport and macroautophagy mediated by a novel mechanism
362 involving the proteasome complex through the deubiquitinating activity of PSMD14
363 (Model on Fig. 8). We propose that inhibition of PSDM14 DUB activity by CZM is a new
364 strategy to cause inhibition of the Golgi-to-ER retrograde pathway. Thus, CZM should now
365 be considered a new pharmacological tool to study the impact of Golgi-to-ER retrograde

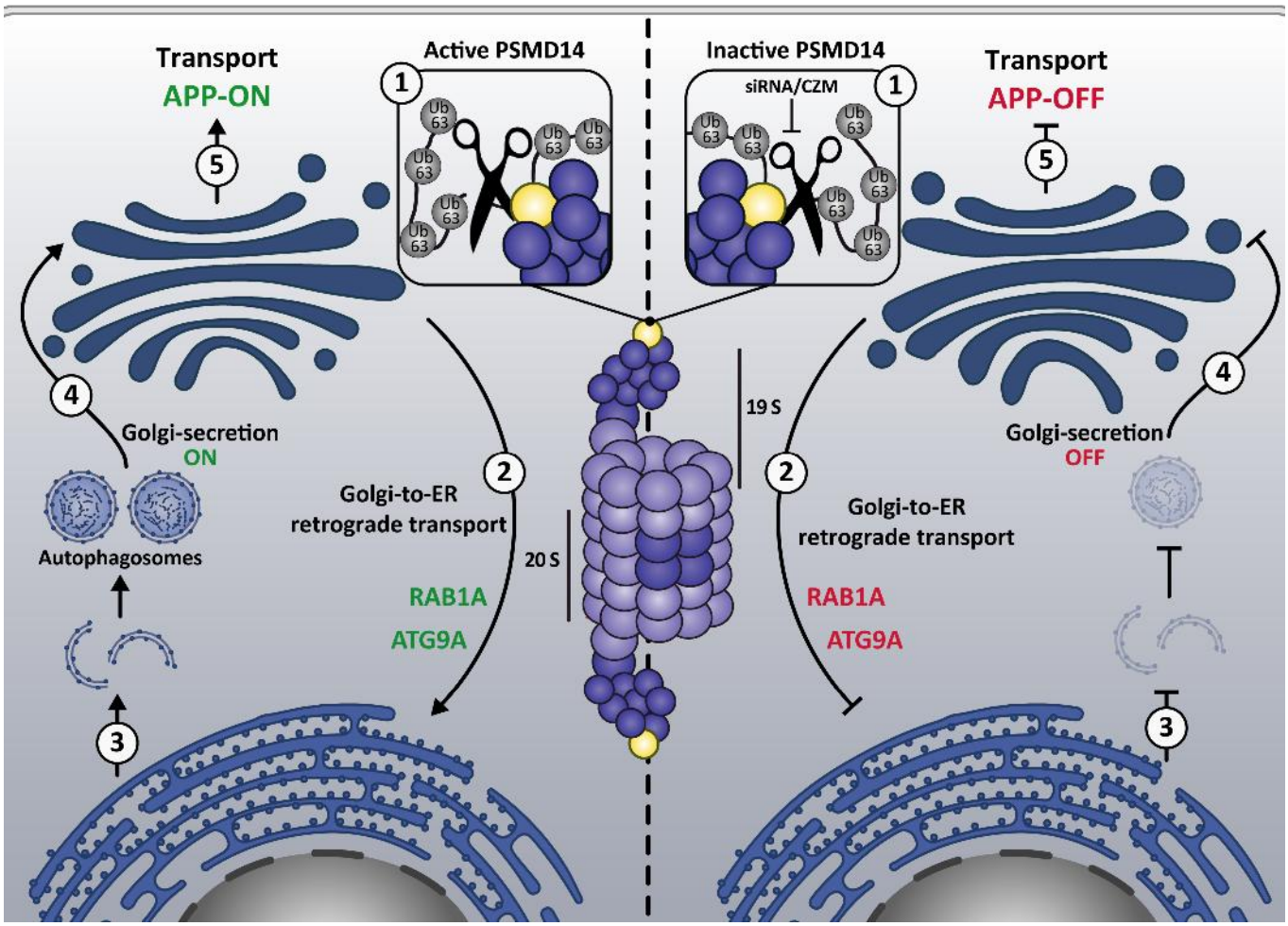
Transport
APP-ON
Active PSMD14
Inactive PSMD14
siRNA/CZM
Transport
APP-OFF
Ub 63
Golgi-secretion
ON
Autophagosomes
Golgi-to-ER
retrograde transport
RAB1A
ATG9A
20 S
19 S
Golgi-secretion
OFF
Golgi-to-ER
retrograde transport
RAB1A
ATG9A

**Figure 8**

366 transport inhibition in other cell biology processes, such as autophagy. Moreover, because
367 CZM was discovered as a new drug for cancer treatment [37], it would be now interesting to
368 investigate whether part of its anti-cancer effects could be the result of inhibiting Golgi-to-
369 ER retrograde pathway. Interestingly, recent studies have shown that PSMD14 is
370 upregulated (mRNA and protein levels) in different tumoral cell types [81,82]. Whether cancer
371 cells are more dependent of Golgi-to-ER retrograde pathway than normal cells, as it
372 happens regarding the mechanisms of protein quality control [83] is still unclear. CZM could
373 offer an interesting tool to evaluate this hypothesis positioning PSMD14 as a promising
374 target for therapeutic intervention.

375 **Materials and Methods**

376 ***Chemical Reagents***

377 Earle's balanced salt solution (EBSS) and the cocktail of protease inhibitors were
378 purchased from Sigma-Aldrich (St. Louis, MO, USA). MG132 was purchased from
379 Millipore (Burlington, MA, USA). Torin-1 was purchased from Tocris Bioscience (Bristol,
380 UK). Dr. Raymond Deshaies from California Institute of Technology (Caltech), CA, USA
381 and Dr. Yuyong Ma from University of California, CA, USA kindly donated Capzimin
382 (CZM).

383 ***Antibodies***

384 We used the following monoclonal antibodies: mouse anti-ubiquitin clone P4D1
385 (Cytoskeleton, Inc, Denver, Co, USA), mouse anti-β-actin clone BA3R (Thermo Fisher
386 Scientific, Waltham, MA, USA), rabbit anti-RAB1A clone D3X9S, mouse anti-GM130
387 clone 35/GM130, rabbit anti-PSMD14 clone D18C7 (Cell Signaling Technology, Danvers,
388 MA, USA) and rabbit anti-ATG9A clone EPR2450(2) (Abcam, Cambridge, UK). We used
389 the following polyclonal antibodies: rabbit anti-ubiquitin (cat: Z0458, Dako, Carpintería,
390 CA, USA), rabbit anti-Giantin (cat: AB24586, Abcam, Cambridge, UK), rabbit anti-LC3
391 (cat: 2775S, Cell Signaling Technology, Danvers, MA, USA), rabbit anti-APP CT695 (cat:
392 51-2700, Thermo Fisher Scientific). Horseradish Peroxidase-conjugated secondary
393 antibodies were purchased from Jackson ImmunoResearch Laboratories (West Grove, PA,
394 USA), and DAPI probe, Alexa and Dylight fluorophore-conjugated secondary antibodies
395 were purchased from Thermo Fisher Scientific.

396 ***Cell Culture***

397 H4 ATCC ® HTB-148™ Homo sapiens brain neuroglioma cells, referred here as H4
398 human neuroglioma cells and HeLa ATCC ® CCL-2™ cells were obtained from the
399 American Type Culture Collection (Manassas, VA, USA). Cell lines were cultured in
400 Dulbecco's modified Eagle's medium (DMEM; Thermo Fisher Scientific) supplemented
401 with 10% (vol/vol) heat-inactivated fetal bovine serum (FBS; Thermo Fisher Scientific),
402 and penicillin/streptomycin (Thermo Fisher Scientific), in a 5% $CO_2$ atmosphere at 37°C.
403 The generation of the H4 stable cell line expressing hemagglutinin-tagged $APP_{695}$-F/P-
404 D/A-EGFP (APP-EGFP) and the HeLa stable cell line expressing KDELR1-GFP were
405 previously reported [32,44,84]. Stably transfected cells were maintained in culture medium
406 supplemented with 100 µg/ml G418. Cells were grown to sub confluence and then treated
407 with drugs or transfected with siRNAs for further western blot and immunofluorescence
408 analyses. Nutrient starvation assays were performed in the presence of EBSS. Assays to
409 detect *Mycoplasm* were performed periodically.

410 ***High Content siRNA Transfection and Imaging***

411 The primary siRNA screen for levels of APP-EGFP were performed in duplicates with our
412 custom-assembled "Ubiquitinome" siRNA library, which consists of 1,187 SMARTpools
413 siRNAs targeting all known and assumed components of the ubiquitin and ubiquitin-like
414 systems in 96-well format, previously reported [30,31]. The H4 cells stably expressing APP-
415 EGFP were reverse transfected [30,31] in µClear bottom 96-well plates (Greiner Bio-One,
416 Kremsmünster, Austria) with ON- TARGETplus SMARTpools siRNAs (GE Dharmacon,
417 Lafayette, CO, USA). Additionally, ON-TARGETplus Non-targeting pool (NT siRNA)
418 was used together with untransfected cells (Mock) as neutral control; siRNA against GFP
419 (GFP siRNA) was used as positive control for APP downregulation. Briefly, 10 µl siRNA
420 (200 nM) were stamped from 96-well plates of the library on to µClear bottom 96 well
421 plates. Thereafter, 10 µl of Opti-MEM I Reduced Serum Medium (Thermo Fisher
422 Scientific) containing Lipofectamine RNAiMAX transfection reagent (Thermo Fisher
423 Scientific) was added to the siRNA (dilution 1:50). Plates were shaken at 900 rpm for 1
424 min followed by incubation for 20 min at room temperature. During this incubation cells
425 were resuspended in DMEM supplemented with 10% (vol/vol) FBS and 1x Normocin
426 (InvivoGen, San Diego, CA, USA) and 6,000 cells were dispensed onto each well loaded

427 with medium for a final siRNA concentration of 20 nM. Plates were incubated for 72 h and
428 further prepared for high content measurement.
429 After transfection, cells were stained using 100 µl of reagent per step, dispensed by the
430 automated reagent dispenser XPP-721 (fluidX, Manchester, UK), according to the
431 following protocol: two washes in phosphate buffered saline (PBS); fixation in 3.7%
432 (vol/vol) paraformaldehyde for 10 min; one wash in PBS; incubation with 0.2% (vol/vol)
433 Triton X-100 in PBS for 10 min; two washes in PBS; incubation with 0.1 µg/ml DAPI for 5
434 min; two washes with PBS. Finally, 100 µl of PBS were left in each well. Images were
435 acquired and analyzed using the automated microscope IN Cell 2000 Analyzer (GE
436 Healthcare, Little Chalfont, UK). Images of six randomized fields per well having ~ 600
437 cells each were acquired, and further analyzed the total fluorescence intensity in n > 2,000
438 cells per condition. A secondary siRNA screening was performed in triplicate targeting the
439 35 most responsive hits, using each single siRNA duplex derived from the SMARTpools
440 used in the primary siRNA screening.
441 ***siRNA Transfection for the siRNA Screening Validation Stage***
442 Four single siRNA sequences targeting human PSMD14 (Accession number:
443 NM_005805), derived from the ON-TARGETplus SMARTpool used in the siRNA
444 Screening (Suppl. Fig. 7) were purchased from GE Dharmacon (Lafayette, CO, USA).
445 siRNA transfections were carried out in 60 mm tissue culture plates using the
446 Lipofectamine RNAiMax transfection reagent (Thermo Fisher Scientific) according to the
447 manufacturer's protocol, and after 72 h cells were collected for further analysis.
448 ***RNA isolation and RT-qPCR Analysis***
449 Total RNA extraction from H4 cells was carried out using the E.Z.N.A.® Total RNA Kit I
450 (Omega Biotek, Norcross, GA, USA), and either purity (260nm/280nm ratio and
451 260nm/230nm ratio) and quantity (260nm absorbance) were determined by
452 spectrophotometry using NanoVue Spectrophotometer (GE Healthcare). The cDNA
453 synthesis was performed from 2.5 µg of total RNA and oligo-dT and MMLV reverse
454 transcriptase (Promega, Madison, WI, USA) according to supplier instructions. Specific
455 primer pairs for *tbp* (NM_003194), *psmd14* (NM_005805) and *app* (NM_000484) human
456 genes were designed for quantitative reverse transcription PCR on cDNA template (RT-
457 qPCR) (Suppl. Fig. 8). First, the specificity of amplicons was verified by cloning and

| | Sequence |
|---|---|
| **siRNA #1** | (5´-GAACAAGUCUAUAUCUCUU-3´) |
| **siRNA #2** | (5´-GGCAUUAAUUCAUGGACUA-3´) |
| **siRNA #3** | (5´-AGAGUUGGAUGGAAGGUUU-3´) |
| **siRNA #4** | (5´-GAUGGUUGUUGGUUGGUAU-3´) |

# Supplementary Figure 7

| Target | Sequence |
| --- | --- |
| **hTBP1** | f(5´-TAGTCCAATGATGCCTTACG-3´)<br>r(5´-TGGTCAGAGTTTGAGAATGG-3´) |
| **hPSMD14** | f(5´-ACCTTAAGAGTTGTAGTTACTGACC-3´)<br>r(5´-TTTAACAGTGCCAGGGAAGAG-3´) |
| **hAPP** | f(5´-CCTAAAGCATTTCGAGCATG-3´)<br>r(5´-GTTTCCGTAACTGATCCTTG-3´) |

# Supplementary Figure 8

458 sequencing, including *tbp* (223bp), *psmd14* (150bp) and *app* (247bp). mRNA levels were
459 quantified in cDNA by qPCR with GoTaq qPCR Master Mix (Promega) according to
460 supplier's instructions in a Mx3000 Real-Time Thermocycler (Stratagene, San Diego, CA,
461 USA). In a 40 cycles PCR reaction, each cycle consisted in 20 s at 94°C, 15 s at 55°C and
462 15 s at 72°C, followed by a final heating at 95°C, revealing melting curves that confirmed
463 single amplification products. All analyses were performed in triplicate. The expression
464 level of each gene was normalized to *tbp* expression as reference gene using exon-spanning
465 primers to control for genomic DNA contamination since no DNAse treatment of total
466 RNA was included. RT-qPCR assays were analyzed with 2(-ΔΔCt) method [85] via MxPro
467 software (Stratagene) and expressed as relative quantity to normalizer [86].

468 ***Preparation of protein extracts, Electrophoresis, SDS-PAGE and Western Blot analysis***

469 Cells were washed in ice-cold Phosphate Buffered Saline (PBS) and lysed at 4°C in lysis
470 buffer (50 mM Tris-HCl pH 7.4, 150 mM NaCl, 1 mM EDTA, 1% (vol/vol) Triton X-100)
471 supplemented with a cocktail of protease inhibitors (Sigma-Aldrich). All lysates were
472 cleared by centrifugation at 16,000 x *g* for 20 min at 4°C, and protein concentration was
473 determined with a protein assay dye reagent (Bio-Rad Laboratories, Hercules, CA, USA).
474 Samples with an equivalent amount of protein were boiled for 5 min with Laemmli SDS-
475 PAGE sample buffer, and then analyzed by SDS-PAGE. Proteins were electroblotted onto
476 nitrocellulose membranes, blocked by incubation for 30 min in PBS containing 5% (wt/vol)
477 free-fat dry milk, and incubated sequentially with primary and secondary antibodies, both
478 diluted in blocking solution, for 1 h at room temperature, or overnight at 4°C.
479 Chemiluminescence protein detection was performed using SuperSignal West Pico
480 (Thermo Fisher Scientific). β-Actin was used as an internal loading control.

481 ***In vitro Proteasomal Activity Assay***

482 Proteasome activity was quantitatively assessed in H4 cell extracts using the β5-selective
483 fluorogenic substrate succinyl-leucine-leucine-valine-tyrosine-4-methyl-7-courmarylamide
484 (Suc-LLVY-AMC, Calbiochem, Burlington, MA, USA) using an adapted protocol [87].
485 Briefly, cells were left untreated or treated for 4 h with different amounts of CZM (between
486 2 and 10 μM) or with 10 μM MG132. Cells were lysed in lysis buffer (20 mM Tris-HCl,
487 pH 7.2, 1 mM EDTA, 1 mM dithiothreitol (DTT) and 0.1% (vol/vol) Nonidet P-40)
488 supplemented with a cocktail of protease inhibitors (Sigma-Aldrich). Lysates were cleared

489 by centrifugation at 16,000 x *g* for 20 min at 4°C, and protein concentration was
490 determined with a protein assay dye reagent (Bio-Rad Laboratories, Hercules, CA, USA).
491 Soluble extracts (20 µg) were incubated for 60 min at 37°C in proteasome assay buffer (50
492 mM Tris-HCl, pH 7.2, 1 mM DTT, 0,5 mM EDTA and 100 µM Suc-LLVY-AMC) all
493 dispensed in triplicate into a 96-well black opaque plate (Nunc, Thermo Fisher Scientific).
494 Proteasome activity was measured by monitoring the production of free AMC using a
495 Synergy HT Multi-detection Microplate Reader (BioTek Instruments, VT, USA) with
496 excitation and emission wavelengths of 360 nm and 460 nm, respectively, and the data
497 were obtained by Gen5 Version 2.09.1 data analysis software. Statistical significance was
498 determined by One-Way ANOVA, followed by Dunnett's test. Value of P <0,01(**) and P
499 <0,001(***) were regarded as statistically significant and is indicated in the figure.

500 ***Immunofluorescence***

501 Cells grown on glass coverslips were washed with PBS and fixed in 4% (vol/vol)
502 paraformaldehyde for 30 min at room temperature. After fixation, cells were washed in
503 PBS and permeabilized with 0.2% (vol/vol) Triton X-100 in PBS for 10 min at room
504 temperature. Cells were incubated with the indicated primary antibodies diluted in
505 immunofluorescence buffer (PBS containing 10% (vol/vol) FBS and 0.1% (wt/vol)
506 Saponin) for 30 min at 37°C. Coverslips were washed in PBS and incubated with the
507 corresponding Alexa-conjugated secondary antibody diluted in immunofluorescence buffer
508 for 30 min at 37°C. For nuclei staining, cells were washed with PBS and incubated for 10
509 min at room temperature with 0.1 mg/ml DAPI. After the final wash, coverslips were
510 mounted onto glass slides with Fluoromount-G (SouthernBiotech, Birmingham, AL, USA).

511 ***Fluorescence Microscopy***

512 Images of fixed cells were acquired by using a TCS SP8 laser-scanning confocal
513 microscope (Leica Microsystems, Wetzlar, Germany) equipped with a 63X oil immersion
514 objective (1.4 NA), 405 nm, 488 nm and 561 nm laser lines, with Photomultiplier (PMT), a
515 hybrid detector system (Leica HyD) and the Leica Application Suite LAS X software. For
516 quantification of fluorescent signals, 8-bit images were acquired under identical settings
517 avoiding signal saturation and corrected for background signal on each image. The
518 corrected fluorescent signal in each cell of each image was used in Image J (version 1.44o;
519 Wayne Rasband, NIH, http://imagej.nih.gov) to determine the total integrated pixel

520 intensity per cell area. Colocalization analyses were performed with sets of
521 immunofluorescence images (Z-stack, with 0.2 μm intervals) of the same cells for each
522 marker. Quantification of the acquired images was performed with the ICY software
523 (Quantitative Image Analysis Unit, Institut Pasteur, http://icy.bioimageanalysis.org/) using
524 protocols plugin to create a pipeline to analyze the images in batch, active contours plugin
525 was used to perform the cell segmentation, hk-means plugin was used for threshold
526 detection, wavelet spot detector plugin was used for spot detection and colocalization
527 studio plugin for colocalization analysis.
528 For live cell imaging assays, H4 cells were grown in glass bottom culture dishes (MatTek
529 Corporation, Ashland, MA, USA) and transiently transfected for 48-h with KDELR-
530 VSVG-YFP, using TransIT-LT1 Transfection Reagent (Mirus Bio LLC, Madison, Wi,
531 USA) according to the manufacturer's protocol. Before the live cell imaging assay, the
532 culture medium was replaced with phenol red-free DMEM supplemented with HEPES
533 (10mM, pH 7.4), and the cells were treated with CZM (10μM) at 32°C in a controlled
534 temperature chamber in the TCS SP8 laser-scanning confocal microscope. Cells were kept
535 at 32°C to allow KDELR-VSVG-YFP localization on the Golgi, followed by a shift in
536 temperature to 40°C. Imaging was done with a 63X oil immersion objective (1.4 NA),
537 running the Leica Application Suite LAS X software, acquiring 8-bit images at 1-min
538 interval for 15 min at 40°C (488 laser for excitation; HyD: 510-550 nm; 1024×1024 pixels;
539 frame average 1). Quantification of the acquired images was performed with the
540 MetaMorph Software version 7.0.
541 ***3D Golgi Reconstruction and Golgi Volume and Area Measurements***
542 H4 and HeLa cells stably expressing KDELR1-GFP, under the specified conditions, were
543 fixed and immunostained with anti-GM130 or anti-Giantin, respectively. The
544 immunofluorescence protocol was performed as described above to visualize the Golgi
545 structure. For Golgi volume and area measurements, Z-stack (250 nm) fluorescence images
546 were acquired by using a TCS SP8 laser-scanning confocal microscope (Leica
547 Microsystems, Wetzlar, Germany) equipped with a 63X oil immersion objective (1.4 NA)
548 running the Leica Application Suite LAS X software. Images were then processed with
549 ImageJ software version FIJI to remove the background by using threshold. The
550 thresholded images were then visualized using the "3D Viewer" plugin. The Golgi volume

551 was quantified using ImageJ software version FIJI by setting a thresholded region to select
552 only the Golgi fluorescence. Then, the Golgi structures were separated by ROI (Regions of
553 Interest) and the individual Golgi volume was measured with the plugin "Voxel Counting".
554 The Golgi volume in $\mu m^3$ was determined by the number of voxels contained in the stack of
555 images (voxel 0.2x0.2x0.25 nm). The Golgi Area was quantified using ICY software and
556 the Golgi marker GM130 was used to determine the ROI. To separate the specific signal
557 from background "k means threshold" plugin was used, using the same threshold level to
558 all images. Data analysis was performed using GraphPad Prism 6 (GraphPad Software, La
559 Jolla, CA, USA) and the results represented in graphs depicting the mean ± SEM of at least
560 20 cells. Statistical significance of the data was determined with Student's T-test. The value
561 of P <0,001(***) was regarded as statistically significant and is indicated in the respective
562 figures.

563 ***Densitometric Quantification and Statistical Analysis***

564 The amount of immunoblot signal was estimated using Image J software version 1.48v
565 (Wayne Rasband, NIH, http://imagej.nih.gov). For each condition, protein bands were
566 quantified from at least three independent experiments in order to ensure adequate
567 statistical power. Data analysis was performed using Microsoft Excel 2013 for Windows
568 (Redmond, WA, USA) or GraphPad Prism 6. Results are represented in graphs depicting
569 the mean ± standard deviation. Statistical significance of data comparisons from two groups
570 comparisons was determined with Student's T-test for parametric data. Values of P <0.05
571 (*), P <0.01 (**), P <0.001 (***) were regarded as statistically significant and are indicated
572 in the figures. Statistical significance of data from many groups was analyzed using One-
573 Way ANOVA, followed by Tukey's test in order to evaluate pair-wise comparisons. The
574 value of P <0.05 was regarded as statistically significant and indicated in the figure in
575 different letters above bars mean.

576 **Author Contributions:** Conceptualization, B.H.A., R.F.A. and B.P.V.; Experimental
577 design, B.H.A., R.F.A., M.G.A., C.J., and B.P.V.; Execution of experiments, B.H.A.,
578 R.F.A., B.S., C.K., V.G.E., A.M.E., C.T.C., Data analysis, B.H.A., C.K., G.A.E., V.G.E.,
579 C.Y., H.S., A.M.E., C.T.C. Reagents, Materials, and Analysis tools, V.G.E., H.S., B.S.,
580 A.S., K.G., M.G.A., C.J., H.R.T., R.F.A. and B.P.V. writing—original draft preparation,

B.H.A., R.F.A. and B.P.V.; writing—review and editing, B.H.A., B.S., A.S., K.B., M.G.A., C.J., R.F.A., H.R.T and B.P.V.; funding acquisition, B.P.V., R.F.A and H.R.T.

**Funding Statement:** This work was funded by Fondo Nacional de Desarrollo Científico y Tecnológico of Chile (FONDECYT; http://www.conicyt.cl/fondecyt) No. 1171649 to B.P.V. & No. 11150532 to R.F.A.; Associative Investigation Program (PIA; https://www.conicyt.cl/pia) including No. ACT-172066 to B.P.V. &No. AFB-170005 to B.P.V.; Academy Insertion Program (PAI; https://www.conicyt.cl/pai) No. 79150075 to R.F.A.; Fondo de Equipamiento Científico y Tecnológico of Chile (FONDEQUIP; http://www.conicyt.cl/fondequip) No. EQM150118 to B.P.V.; Cooperation International Programme (CONICYT-RCUK; https://www.conicyt.cl/pci) No. DPI20140068 to B.P.V.; B.H.A, G.A.E., and V.G.E. were supported by National Ph.D Fellowships No. 21130315, 201110746 and 21130511 respectively (CONICYT; https://www.conicyt.cl/becasconicyt); Programa de Mejoramiento de la Calidad y la Equidad de la Educación superior, MECESUP AUS1203 and Vicerrectoría de Investigación de la Universidad Austral de Chile No. D #2015-02 to B.H.A., D #2013-07 to A.E.G. and D #2015-05 to V.G.E. The funders had no role in study design, data collection and analysis, decision to publish, or preparation of the manuscript.

**Acknowledgments:** We thank Gonzalo Astroza (Universidad Austral de Chile) and Ellis Jaffray (GRE, University of Dundee) for technical assistance. Dr. Raymond Deshaies (Division of Biology & Biological Engineering, California Institute of Technology) & Dr. Yuyong Ma (Department of Chemistry and Biochemistry, University of California) for proving Capzimin for this study.

**Conflicts of Interest:** The authors declare no conflict of interest.

**Abbreviations**

APP: Amyloid Precursor Protein

CZM: Capzimin

DUB: Deubiquitinating enzyme

EBSS: Earle's balanced salt solution

EGFP: Enhanced Green Fluorescent Protein

610 ER: Endoplasmic Reticulum
611 FBS: Fetal bovine serum
612 GFP: Green Fluorescent Protein
613 GM130: Golgi matrix protein GM130
614 HCS: High-Content siRNA Screening
615 ILV: intraluminal vesicle
616 K: Lysine residue
617 KDELR1: KDEL (Lys-Asp-Glu-Leu) Receptor 1
618 KD: Knock-down
619 LC3B: Microtubule-associated protein 1 light chain 3B
620 mTORC: mammalian target of rapamycin complex
621 MVB: multivesicular body
622 NT: Non-Target
623 PBS: Phosphate Buffered Saline
624 PCR: Polymerase Chain Reaction
625 PTM: Post-translational Modification
626 RP: 19S regulatory particle
627 RT-qPCR: Quantitative reverse transcription PCR
628 SENP: SUMO-specific protease
629 siRNA: Small interfering RNA
630 Ub: Ubiquitin
631 UBD: Ub-binding domain
632 ULK1: unc-51-like kinase 1
633 VSVG: Vesicular Stomatitis Virus G
634 YFP: Yellow Fluorescent Protein

635 **Figure Legends**

636 **Figure 1. High-Content siRNA Screening assay revealed PSMD14 as a novel regulator**
637 **of APP levels. (A)** Graphical distribution of the targets evaluated in the primary High
638 Content siRNA screening using the siRNA "ubiquitinome" library in H4 cells. **(B)**
639 Quantification of the total fluorescence intensity of reporter APP-EGFP cells transfected
640 for 72 h with NT siRNA and EGFP siRNA. Bars represent the mean ± SD with a statistical
641 Z factor = 0.69. **(C)** High content images (20X) captured in reporter APP-EGFP cells
642 transfected for 72 h with NT siRNA and EGFP siRNA. **(D)** Graphical representation of
643 total fluorescence intensity of all 1,187 genes analyzed in primary siRNA screening with
644 the reporter APP-EGFP cells. PSMD14 appears indicated as the top hit. **(E)** High content
645 images (20X) in pseudo color of reporter APP-EGFP cells transfected for 72 h with siRNA
646 SMARTpool targeted against PSMD14 (PSMD14 siRNA) in comparison to cells
647 transfected with NT siRNA. Scale Bar of the images indicates the scale of fluorescence
648 intensity.

649 **Figure 2. PSMD14 is validated as a regulator of the endogenous APP levels.**
650 **(A)** Protein extracts of parental H4 cells either untransfected (Mock), transfected with NT
651 siRNA, or transfected with four different PSMD14 siRNA sequences for 72 h were
652 analyzed by western blot. Polyclonal antibodies to endogenous APP (CT695) and to
653 Ubiquitin, and monoclonal antibodies to PSMD14 (clone D18C7) and to β-actin (clone
654 BA3R), were tested. The position of molecular mass markers are indicated on the left.
655 Densitometric quantification of the levels of endogenous APP protein levels **(B)** and
656 PSMD14 **(C)** in H4 cells transfected with PSMD14 siRNA#1, compared to untransfected
657 cells (Mock). Statistical significance was determined by Student's t-test. Bars represent the
658 mean ± SD of biological replicates (APP n =5; PSMD14 n=4). **P <0.01 and ***P <0.001.
659 **(D)** mRNA levels of *psmd14* and **(E)** mRNA levels of *app* were measured using RT-qPCR
660 from parental H4 cells transfected for 72 h. All data were normalized for TATA binding
661 protein expression in either untransfected cells (Mock), cells transfected with NT siRNA or
662 cells transfected with four different PSMD14 siRNAs duplexes. Statistical significance was
663 determined by One-Way ANOVA, followed by Tukey's test. Bars represent the mean ± SD

664 of biological replicates (*psmd14* n=3; *app* n=3). Different letters above the mean bars apply
665 to significant differences between groups P <0.01.

666 **Figure 3. Acute inhibition of PSMD14 by CZM shows a similar phenotype as PSMD14**
667 **KD on the levels of APP and high molecular weight Ub conjugates.**
668 **(A)** Schematic diagram of the molecular targets of Capzimin and MG132 in the 19S RP
669 and 20S catalytic core of the proteasome, respectively. **(B)** Parental H4 cells were treated
670 either with vehicle (DMSO; Control), or increasing doses of CZM for 4 h, or MG132 for 6
671 h. Protein extracts were analyzed by western blot with a polyclonal antibody to endogenous
672 APP. Monoclonal antibody to β-actin (clone BA3R) was used as a loading control. The
673 position of molecular mass markers is indicated on the left. **(C)** Densitometric
674 quantification of APP protein levels as shown in (D). Statistical significance was
675 determined by One-Way ANOVA, followed by Tukey's test. Bars represent the mean ± SD
676 of biological replicates (n=4). Different letters above the mean bars apply to significant
677 differences between groups P <0.05. **(D)** Parental H4 cells were treated as in (B), and the
678 protein extracts were analyzed by western blot with a polyclonal antibody to Ub.
679 Monoclonal antibody to β-actin (clone BA3R) was used as a loading control. The position
680 of molecular mass markers is indicated on the left. **(E)** Immunofluorescence microscopy
681 images of the cellular localization of Ub in parental H4 cells treated with either the vehicle
682 (DMSO; Control), CZM for 4 h or MG132 for 6 h. Cells were fixed, permeabilized and
683 stained with a mouse monoclonal antibody to Ub (clone P4D1) followed by Alexa-488-
684 conjugated donkey anti-mouse IgG. Scale bar, 10 μm. (n=3).

685 **Figure 4. Acute inhibition of PSMD14 by CZM triggers the accumulation of APP in a**
686 **swollen Golgi apparatus.**
687 Immunofluorescence analysis of endogenous APP in H4 parental cells treated either with
688 the vehicle (DMSO; Control) **(A-C)** or CZM **(D-F)** for 4 h. Cells were fixed,
689 permeabilized, and double stained with a rabbit polyclonal antibody to APP (CT695) (A
690 and D) and a mouse monoclonal antibody to GM130 (clone35/GM130) (B and E), followed
691 by Alexa-594-conjugated donkey anti-Rabbit IgG and Alexa-488-conjugated donkey anti-
692 Mouse IgG. Merging of the images generated the third picture (C and F). Scale bar, 10 μm.
693 **(G)** Quantitative analysis of the mean of total fluorescence intensity of APP upon treatment

694 with CZM, in comparison to control cells. The statistical significance was determined by
695 Student's t-test. Bars represent the mean ± SD of the fluorescent signal per cell area (n=43
696 cells). ***P <0.001. **(H)** Quantitative analysis of the fraction of APP colocalizing with
697 GM130 under CZM treatment and compared to control cells. Statistical significance was
698 determined by Student's t-test. Bars represent the mean ± SD of the fluorescent signal per cell
699 area (n=43 cells). ***P <0.001. **(I)** Quantitative analysis of the cell area. Statistical significance
700 was determined by Student's t-test. Bars represent the mean ± SD of the cell area (n=43 cells)
701 **P <0.001. **(J)** Immunofluorescence microscopy analysis of GM130 in parental H4 cells
702 treated either with the vehicle (DMSO; Control) or CZM for 4 h. Cells were fixed,
703 permeabilized and stained with mouse monoclonal antibody to GM130 (clone 35/GM130)
704 followed by Alexa-488-conjugated donkey anti-mouse IgG, and nuclei were stained with
705 DAPI. Scale bar, 10 µm. **(K)** 3D reconstructions of the Golgi apparatus using GM130 as
706 Golgi marker were generated from Z-stacks (250 nm). **(L)** Golgi Volume was measured
707 from 3D reconstructions as shown in (K). Statistical significance was determined by
708 Student's t-test. Bars represent the means ± SEM (n=20 cells). *** P <0.001.

709 **Figure 5. The PSMD14 DUB inhibitor CZM impairs Golgi-to-ER retrograde**
710 **transport.**

711 **(A)** 3D reconstructions of the Golgi apparatus using Giantin as Golgi marker were
712 generated from Z-stacks (250 nm) obtained from HeLa cells stably expressing KDELR1-
713 GFP treated for 90 min either with vehicle (DMSO; Control), CZM or MG132. **(B)** Golgi
714 volume was measured from 3D reconstructions as shown in (A). Statistical significance
715 was determined by Student's t-test. Bars represent the means ± SEM (n=30 cells). *** P
716 <0.001. **(C)** HeLa cells stably expressing KDELR1-GFP were treated for 90 min either
717 with vehicle (DMSO; Control), CZM or MG132. Cells were fixed and representative
718 confocal images were acquired. **(D)** Measurement of Giantin and total KDELR1-GFP total
719 fluorescent intensity. Statistical significance was determined by Student`s t-test. Bars
720 represent the means ± SEM (n=34 cells). *** P <0.001. **(E)** H4 cells were transiently
721 transfected to express the thermo-sensitive retrograde transport reporter KDELR-VSVG-
722 YFP. Cells were kept at 32°C to allow KDELR-VSVG-YFP localization at the Golgi. Cells
723 were then shifted to 40°C (restrictive temperature) and images acquired at 1 min interval
724 for 15 min. **(F)** Quantitative image analysis was performed to measure the integrated

725 fluorescence of KDELR-VSVG-YFP at the Golgi at 1 min interval for 15 min. Statistical
726 significance was determined by Student`s t-test. Bars represent the mean ± SEM (n=3
727 cells). *p<0.05

728 **Figure 6. Inhibition of autophagosome formation by CZM.**
729 Immunofluorescence microscopy analysis of the subcellular localization of endogenous
730 LC3B in parental H4 cells treated with either the vehicle (DMSO; Control) **(A)**, EBSS for 4
731 h **(B),** CZM for 6 h **(D)** or Torin-1 for 4 h **(E)**. EBSS **(C)** and Torin-1 **(F)** were tested using
732 a 2-h pretreatment with CZM followed by the treatment with EBSS or Torin-1 for 4 h in the
733 presence of CZM. Cells were fixed, permeabilized and stained with a rabbit polyclonal
734 antibody to LC3B followed by Alexa-594-conjugated donkey anti-Rabbit IgG, and nuclei
735 were stained with DAPI. Scale bar 10 μm. **(G)** Quantification of the puncta positive to
736 LC3B. Statistical significance was determined by One-Way ANOVA, followed by Tukey's
737 test. Bars represent the mean ± SEM (n=50 cells). Different letters above the mean bars
738 indicate the significant differences between groups P <0.05. **(H)** Protein extracts from
739 parental H4 cells treated as in (A-F) were analyzed by western blot with a rabbit polyclonal
740 antibody to LC3B. Monoclonal antibody to β-actin (clone BA3R) was used as a loading
741 control. The position of molecular mass markers is indicated on the left. **(I)** Densitometric
742 quantification of LC3B-I levels and **(J)** LC3B-II levels. Statistical significance was
743 determined by One-Way ANOVA, followed by Tukey's test. Bars represent the mean ±
744 SEM of biological replicates (LC3B-I n=3; LC3B-II n=3). Different letters above the mean
745 bars indicate the significant differences between groups P <0.05.

746 **Figure 7. Redistribution of RAB1A and ATG9A to the Golgi apparatus with CZM.**
747 **(A)** Immunofluorescence analysis of endogenous RAB1A and ATG9A in H4 parental cells
748 treated for 4 h either with the vehicle (DMSO; Control) (left panel) or CZM (right panel).
749 Cells were fixed, permeabilized, and stained with a rabbit monoclonal antibody to RAB1A
750 (clone D3X9S) (upper panel) and a rabbit monoclonal antibody to ATG9A (clone
751 EPR2450(2)) (lower panel), followed by Alexa-594-conjugated donkey anti-Rabbit IgG.
752 Scale Bar, 10 μm. (B) Quantitative analysis of the fluorescence intensity of RAB1A upon
753 treatment with CZM, in comparison to control cells. Statistical significance was determined
754 by Student's t-test. Bars represent the mean ± SEM of the fluorescent signal per cell area

755 (n=227 cells). **P <0.01; ***P < 0.001; n.s., not significant. (C) Quantitative analysis of
756 the fluorescence intensity of ATG9A upon treatment with CZM, in comparison to control
757 cells. Statistical significance was determined by Student's t-test. Bars represent the mean ±
758 SEM of the fluorescent signal per cell area (n=95 cells). *P< 0.05; ***P < 0.001; n.s., not
759 significant.

760 **Figure 8. Model of mechanism underlying regulation of protein membrane trafficking**
761 **and macroautophagy by the proteasome 19S RP PSMD14 DUB activity.** The model
762 depicts the closed interplay between membrane transport and macroautophagy by a novel
763 mechanism involving the proteasome complex through the deubiquitinating activity of
764 PSMD14. We propose that active PSMD14 and their K63-Ub chains (1, left panel)
765 positively regulate Golgi-to-ER retrograde transport (2, left panel), pathway implicated in
766 the retrieval of key proteins for autophagosome biogenesis and macroautophagy (3, left
767 panel). Reduction of free K63-Ub chains by inactive PSM14 (1, right panel) results on the
768 blockage of Golgi-to-ER retrograde transport (2, right panel) causing the accumulation of
769 ATG9A and RAB1A at the Golgi apparatus. Thus, blockage of Golgi-to-ER retrograde
770 transport inhibits the biogenesis of autophagosomes and macroautophagy (3, right panel).
771 Macroautophagy has been recently demonstrated to act as a potent positive regulator of
772 protein transport from the Golgi apparatus to the cell surface (Golgi-secretion ON; 4, left
773 panel). Thus, inhibition of macroautophagy upon inactive PSMD14 (siRNA/CZM) blocks
774 protein transport from the Golgi apparatus to the cell surface (Golgi-secretion OFF)
775 explaining the effect on APP transport (5 left and 5 right).

776 **Bibliography**


777 1. Shinde, S. R. & Maddika, S. Post translational modifications of Rab GTPases. *Small*
778 *GTPases* 9, 49–56 (2018).
779 2. Luo, P. M. & Boyce, M. Directing Traffic: Regulation of COPI Transport by Post-
780 translational Modifications. *Front. Cell Dev. Biol.* 7, 190 (2019).
781 3. Li, M. *et al.* Mono- versus polyubiquitination: differential control of p53 fate by
782 Mdm2. *Science* 302, 1972–1975 (2003).
783 4. Komander, D. & Rape, M. The ubiquitin code. *Annu. Rev. Biochem.* 81, 203–229
784 (2012).
785 5. Foot, N., Henshall, T. & Kumar, S. Ubiquitination and the regulation of membrane
786 proteins. *Physiol. Rev.* 97, 253–281 (2017).
787 6. Pelham, H. R. B. Membrane traffic: GGAs sort ubiquitin. *Curr. Biol.* 14, R357–9
788 (2004).
789 7. Yang, B. & Kumar, S. Nedd4 and Nedd4-2: closely related ubiquitin-protein ligases
790 with distinct physiological functions. *Cell Death Differ.* 17, 68–77 (2010).
791 8. Tan, J. & Evin, G. B-site APP-cleaving enzyme 1 trafficking and Alzheimer's disease
792 pathogenesis. *J. Neurochem.* 120, 869–880 (2012).
793 9. Raiborg, C. & Stenmark, H. The ESCRT machinery in endosomal sorting of
794 ubiquitylated membrane proteins. *Nature* 458, 445–452 (2009).
795 10. Ren, X. & Hurley, J. H. VHS domains of ESCRT-0 cooperate in high-avidity binding
796 to polyubiquitinated cargo. *EMBO J.* 29, 1045–1054 (2010).
797 11. Clague, M. J., Liu, H. & Urbé, S. Governance of endocytic trafficking and signaling by
798 reversible ubiquitylation. *Dev. Cell* 23, 457–467 (2012).
799 12. Haglund, K., Di Fiore, P. P. & Dikic, I. Distinct monoubiquitin signals in receptor
800 endocytosis. *Trends Biochem. Sci.* 28, 598–603 (2003).
801 13. Clague, M. J. & Urbé, S. Ubiquitin: same molecule, different degradation pathways.
802 *Cell* 143, 682–685 (2010).
803 14. Kwon, Y. T. & Ciechanover, A. The Ubiquitin Code in the Ubiquitin-Proteasome
804 System and Autophagy. *Trends Biochem. Sci.* 42, 873–886 (2017).
805 15. Ciechanover, A. & Kwon, Y. T. Degradation of misfolded proteins in
806 neurodegenerative diseases: therapeutic targets and strategies. *Exp Mol Med* 47, e147
807 (2015).
808 16. Clague, M. J. & Urbé, S. Endocytosis: the DUB version. *Trends Cell Biol.* 16, 551–
809 559 (2006).
810 17. Komander, D., Clague, M. J. & Urbé, S. Breaking the chains: structure and function of
811 the deubiquitinases. *Nat. Rev. Mol. Cell Biol.* 10, 550–563 (2009).
812 18. Mevissen, T. E. T. & Komander, D. Mechanisms of deubiquitinase specificity and
813 regulation. *Annu. Rev. Biochem.* 86, 159–192 (2017).
814 19. Bienko, M. *et al.* Ubiquitin-binding domains in Y-family polymerases regulate
815 translesion synthesis. *Science* 310, 1821–1824 (2005).
816 20. Bienko, M. *et al.* Regulation of translesion synthesis DNA polymerase eta by
817 monoubiquitination. *Mol. Cell* 37, 396–407 (2010).
818 21. Husnjak, K. & Dikic, I. Ubiquitin-binding proteins: decoders of ubiquitin-mediated
819 cellular functions. *Annu. Rev. Biochem.* 81, 291–322 (2012).

820 22. Lai, A., Sisodia, S. S. & Trowbridge, I. S. Characterization of sorting signals in the
821 beta-amyloid precursor protein cytoplasmic domain. *J. Biol. Chem.* 270, 3565–3573
822 (1995).
823 23. Perez, R. G. *et al.* Mutagenesis identifies new signals for beta-amyloid precursor
824 protein endocytosis, turnover, and the generation of secreted fragments, including
825 Abeta42. *J. Biol. Chem.* 274, 18851–18856 (1999).
826 24. Burgos, P. V. *et al.* Sorting of the Alzheimer's disease amyloid precursor protein
827 mediated by the AP-4 complex. *Dev. Cell* 18, 425–436 (2010).
828 25. Watanabe, T., Hikichi, Y., Willuweit, A., Shintani, Y. & Horiguchi, T. FBL2 regulates
829 amyloid precursor protein (APP) metabolism by promoting ubiquitination-dependent
830 APP degradation and inhibition of APP endocytosis. *J. Neurosci.* 32, 3352–3365
831 (2012).
832 26. El Ayadi, A., Stieren, E. S., Barral, J. M. & Boehning, D. Ubiquilin-1 regulates
833 amyloid precursor protein maturation and degradation by stimulating K63-linked
834 polyubiquitination of lysine 688. *Proc. Natl. Acad. Sci. USA* 109, 13416–13421
835 (2012).
836 27. Morel, E. *et al.* Phosphatidylinositol-3-phosphate regulates sorting and processing of
837 amyloid precursor protein through the endosomal system. *Nat. Commun.* 4, 2250
838 (2013).
839 28. Williamson, R. L. *et al.* Disruption of amyloid precursor protein ubiquitination
840 selectively increases amyloid β (Aβ) 40 levels via presenilin 2-mediated cleavage. *J.*
841 *Biol. Chem.* 292, 19873–19889 (2017).
842 29. Cooper, E. M. *et al.* K63-specific deubiquitination by two JAMM/MPN+ complexes:
843 BRISC-associated Brcc36 and proteasomal Poh1. *EMBO J.* 28, 621–631 (2009).
844 30. Bett, J. S., Ibrahim, A. F. M., Garg, A. K., Rocha, S. & Hay, R. T. SiRNA screening to
845 identify ubiquitin and ubiquitin-like system regulators of biological pathways in
846 cultured mammalian cells. *J. Vis. Exp.* (2014). doi:10.3791/51572
847 31. MacKay, C. *et al.* E3 ubiquitin ligase HOIP attenuates apoptotic cell death induced by
848 cisplatin. *Cancer Res.* 74, 2246–2257 (2014).
849 32. Prabhu, Y. *et al.* Adaptor protein 2-mediated endocytosis of the β-secretase BACE1 is
850 dispensable for amyloid precursor protein processing. *Mol. Biol. Cell* 23, 2339–2351
851 (2012).
852 33. González, A. E. *et al.* Autophagosomes cooperate in the degradation of intracellular C-
853 terminal fragments of the amyloid precursor protein via the MVB/lysosomal pathway.
854 *FASEB J.* 31, 2446–2459 (2017).
855 34. Moffat, J., Reiling, J. H. & Sabatini, D. M. Off-target effects associated with long
856 dsRNAs in Drosophila RNAi screens. *Trends Pharmacol. Sci.* 28, 149–151 (2007).
857 35. Verma, R. *et al.* Role of Rpn11 metalloprotease in deubiquitination and degradation by
858 the 26S proteasome. *Science* 298, 611–615 (2002).
859 36. Yao, T. & Cohen, R. E. A cryptic protease couples deubiquitination and degradation
860 by the proteasome. *Nature* 419, 403–407 (2002).
861 37. Li, J. *et al.* Capzimin is a potent and specific inhibitor of proteasome isopeptidase
862 Rpn11. *Nat. Chem. Biol.* 13, 486–493 (2017).
863 38. Tsubuki, S., Saito, Y., Tomioka, M., Ito, H. & Kawashima, S. Differential inhibition of
864 calpain and proteasome activities by peptidyl aldehydes of di-leucine and tri-leucine. *J.*
865 *Biochem.* 119, 572–576 (1996).

866 39. Kisselev, A. F. & Goldberg, A. L. Proteasome inhibitors: from research tools to drug
867 candidates. *Chem. Biol.* 8, 739–758 (2001).
868 40. Wieland, F. T., Gleason, M. L., Serafini, T. A. & Rothman, J. E. The rate of bulk flow
869 from the endoplasmic reticulum to the cell surface. *Cell* 50, 289–300 (1987).
870 41. Martínez-Menárguez, J. A., Geuze, H. J., Slot, J. W. & Klumperman, J. Vesicular
871 tubular clusters between the ER and Golgi mediate concentration of soluble secretory
872 proteins by exclusion from COPI-coated vesicles. *Cell* 98, 81–90 (1999).
873 42. Klumperman, J. Transport between ER and Golgi. *Curr. Opin. Cell Biol.* 12, 445–449
874 (2000).
875 43. Thor, F., Gautschi, M., Geiger, R. & Helenius, A. Bulk flow revisited: transport of a
876 soluble protein in the secretory pathway. *Traffic* 10, 1819–1830 (2009).
877 44. Cancino, J. *et al.* Control systems of membrane transport at the interface between the
878 endoplasmic reticulum and the Golgi. *Dev. Cell* 30, 280–294 (2014).
879 45. Tenorio, M. J., Luchsinger, C. & Mardones, G. A. Protein kinase A activity is
880 necessary for fission and fusion of Golgi to endoplasmic reticulum retrograde tubules.
881 *PLoS One* 10, e0135260 (2015).
882 46. Hsu, V. W., Shah, N. & Klausner, R. D. A brefeldin A-like phenotype is induced by
883 the overexpression of a human ERD-2-like protein, ELP-1. *Cell* 69, 625–635 (1992).
884 47. Cole, N. B., Ellenberg, J., Song, J., DiEuliis, D. & Lippincott-Schwartz, J. Retrograde
885 transport of Golgi-localized proteins to the ER. *J. Cell Biol.* 140, 1–15 (1998).
886 48. Lewis, M. J., Rayner, J. C. & Pelham, H. R. A novel SNARE complex implicated in
887 vesicle fusion with the endoplasmic reticulum. *EMBO J.* 16, 3017–3024 (1997).
888 49. He, S. *et al.* PtdIns(3)P-bound UVRAG coordinates Golgi-ER retrograde and Atg9
889 transport by differential interactions with the ER tether and the beclin 1 complex. *Nat.*
890 *Cell Biol.* 15, 1206–1219 (2013).
891 50. Lemus, L., Ribas, J. L., Sikorska, N. & Goder, V. An ER-Localized SNARE Protein Is
892 Exported in Specific COPII Vesicles for Autophagosome Biogenesis. *Cell Rep.* 14,
893 1710–1722 (2016).
894 51. Chen, Q. *et al.* ATL3 Is a Tubular ER-Phagy Receptor for GABARAP-Mediated
895 Selective Autophagy. *Curr. Biol.* 29, 846–855.e6 (2019).
896 52. Hao, R. *et al.* Proteasomes activate aggresome disassembly and clearance by producing
897 unanchored ubiquitin chains. *Mol. Cell* 51, 819–828 (2013).
898 53. Nanduri, P., Hao, R., Fitzpatrick, T. & Yao, T.-P. Chaperone-mediated 26S
899 proteasome remodeling facilitates free K63 ubiquitin chain production and aggresome
900 clearance. *J. Biol. Chem.* 290, 9455–9464 (2015).
901 54. Kabeya, Y. *et al.* LC3, a mammalian homologue of yeast Apg8p, is localized in
902 autophagosome membranes after processing. *EMBO J.* 19, 5720–5728 (2000).
903 55. Munafó, D. B. & Colombo, M. I. A novel assay to study autophagy: regulation of
904 autophagosome vacuole size by amino acid deprivation. *J. Cell Sci.* 114, 3619–3629
905 (2001).
906 56. Thoreen, C. C. *et al.* An ATP-competitive mammalian target of rapamycin inhibitor
907 reveals rapamycin-resistant functions of mTORC1. *J. Biol. Chem.* 284, 8023–8032
908 (2009).
909 57. Winslow, A. R. *et al.* α-Synuclein impairs macroautophagy: implications for
910 Parkinson's disease. *J. Cell Biol.* 190, 1023–1037 (2010).
911 58. Webster, C. P. *et al.* The C9orf72 protein interacts with Rab1a and the ULK1 complex
912 to regulate initiation of autophagy. *EMBO J.* 35, 1656–1676 (2016).

913 59. Orsi, A. *et al.* Dynamic and transient interactions of Atg9 with autophagosomes, but
914 not membrane integration, are required for autophagy. *Mol. Biol. Cell* 23, 1860–1873
915 (2012).
916 60. Kishi-Itakura, C., Koyama-Honda, I., Itakura, E. & Mizushima, N. Ultrastructural
917 analysis of autophagosome organization using mammalian autophagy-deficient cells. *J.*
918 *Cell Sci.* 127, 4984 (2014).
919 61. Karanasios, E. *et al.* Autophagy initiation by ULK complex assembly on ER
920 tubulovesicular regions marked by ATG9 vesicles. *Nat. Commun.* 7, 12420 (2016).
921 62. Tapia, D. *et al.* KDEL receptor regulates secretion by lysosome relocation- and
922 autophagy-dependent modulation of lipid-droplet turnover. *Nat. Commun.* 10, 735
923 (2019).
924 63. Iwata, A., Riley, B. E., Johnston, J. A. & Kopito, R. R. HDAC6 and microtubules are
925 required for autophagic degradation of aggregated huntingtin. *J. Biol. Chem.* 280,
926 40282–40292 (2005).
927 64. Ding, W.-X. *et al.* Linking of autophagy to ubiquitin-proteasome system is important
928 for the regulation of endoplasmic reticulum stress and cell viability. *Am. J. Pathol.*
929 171, 513–524 (2007).
930 65. Lan, D., Wang, W., Zhuang, J. & Zhao, Z. Proteasome inhibitor-induced autophagy in
931 PC12 cells overexpressing A53T mutant α-synuclein. *Mol. Med. Rep.* 11, 1655–1660
932 (2015).
933 66. Peng, H. *et al.* Ubiquitylation of p62/sequestosome1 activates its autophagy receptor
934 function and controls selective autophagy upon ubiquitin stress. *Cell Res.* 27, 657–674
935 (2017).
936 67. Milani, M. *et al.* The role of ATF4 stabilization and autophagy in resistance of breast
937 cancer cells treated with Bortezomib. *Cancer Res.* 69, 4415–4423 (2009).
938 68. Albornoz, N., Bustamante, H., Soza, A. & Burgos, P. Cellular responses to proteasome
939 inhibition: molecular mechanisms and beyond. *Int. J. Mol. Sci.* 20, (2019).
940 69. Zhang, J., Liu, J., Norris, A., Grant, B. D. & Wang, X. A novel requirement for
941 ubiquitin-conjugating enzyme UBC-13 in retrograde recycling of MIG-14/Wntless and
942 Wnt signaling. *Mol. Biol. Cell* 29, 2098–2112 (2018).
943 70. Deng, L. *et al.* The ubiquitination of rag A GTPase by RNF152 negatively regulates
944 mTORC1 activation. *Mol. Cell* 58, 804–818 (2015).
945 71. Ji, C. H. *et al.* The N-Degron Pathway Mediates ER-phagy. *Mol. Cell* 75, 1058–
946 1072.e9 (2019).
947 72. Kawaguchi, Y. *et al.* The deacetylase HDAC6 regulates aggresome formation and cell
948 viability in response to misfolded protein stress. *Cell* 115, 727–738 (2003).
949 73. Cohen, M., Stutz, F. & Dargemont, C. Deubiquitination, a new player in Golgi to
950 endoplasmic reticulum retrograde transport. *J. Biol. Chem.* 278, 51989–51992 (2003).
951 74. Millard, S. M. & Wood, S. A. Riding the DUBway: regulation of protein trafficking by
952 deubiquitylating enzymes. *J. Cell Biol.* 173, 463–468 (2006).
953 75. Cohen, M., Stutz, F., Belgareh, N., Haguenauer-Tsapis, R. & Dargemont, C. Ubp3
954 requires a cofactor, Bre5, to specifically de-ubiquitinate the COPII protein, Sec23. *Nat.*
955 *Cell Biol.* 5, 661–667 (2003).
956 76. He, S., O'Connell, D., Zhang, X., Yang, Y. & Liang, C. The intersection of Golgi-ER
957 retrograde and autophagic trafficking. *Autophagy* 10, 180–181 (2014).
958 77. Rinaldi, L. *et al.* Feedback inhibition of cAMP effector signaling by a chaperone-
959 assisted ubiquitin system. *Nat. Commun.* 10, 2572 (2019).

78. Feng, X. *et al.* Ubiquitination of UVRAG by SMURF1 promotes autophagosome maturation and inhibits hepatocellular carcinoma growth. *Autophagy* 15, 1130–1149 (2019).
79. Saitoh, T. *et al.* Atg9a controls dsDNA-driven dynamic translocation of STING and the innate immune response. *Proc. Natl. Acad. Sci. USA* 106, 20842–20846 (2009).
80. Mattera, R., Park, S. Y., De Pace, R., Guardia, C. M. & Bonifacino, J. S. AP-4 mediates export of ATG9A from the trans-Golgi network to promote autophagosome formation. *Proc. Natl. Acad. Sci. USA* 114, E10697–E10706 (2017).
81. Song, Y. *et al.* Blockade of deubiquitylating enzyme Rpn11 triggers apoptosis in multiple myeloma cells and overcomes bortezomib resistance. *Oncogene* 36, 5631–5638 (2017).
82. Wang, C.-H. *et al.* POH1 knockdown induces cancer cell apoptosis via p53 and bim. *Neoplasia* 20, 411–424 (2018).
83. Deshaies, R. J. Proteotoxic crisis, the ubiquitin-proteasome system, and cancer therapy. *BMC Biol.* 12, 94 (2014).
84. Bustamante, H. A. *et al.* Turnover of C99 is controlled by a crosstalk between ERAD and ubiquitin-independent lysosomal degradation in human neuroglioma cells. *PLoS One* 8, e83096 (2013).
85. Livak, K. J. & Schmittgen, T. D. Analysis of relative gene expression data using real-time quantitative PCR and the 2(-Delta Delta C(T)) Method. *Methods* 25, 402–408 (2001).
86. Pfaffl, M. W. A new mathematical model for relative quantification in real-time RT-PCR. *Nucleic Acids Res.* 29, e45 (2001).
87. Mlynarczuk-Bialy, I. *et al.* Biodistribution and efficacy studies of the proteasome inhibitor bsc2118 in a mouse melanoma model. *Transl Oncol* 7, 570–579 (2014).

987 **Supplementary Figures Legends**

988 **Supplementary Figure 1. The PSMD14 DUB inhibitor CZM increases the Golgi**
989 **apparatus area**. Immunofluorescence microscopy analysis of the Golgi area in parental H4
990 cells treated for 4 h either with the vehicle (DMSO; Control) or CZM. The Golgi marker
991 GM130 was used to determine the region of interest in each condition. Statistical
992 significance was determined by Student's t-test. Bars represent the mean ± SEM (n =43
993 cells). ***P <0.001.

994 **Supplementary Figure 2. CZM causes the accumulation of KDELR1-GFP at the Golgi**
995 **apparatus.** HeLa cells expressing KDELR1-GFP were either left untreated or treated with
996 CZM for 30, 60 or 90 min. Cells were fixed and representative confocal images were
997 acquired.

998 **Supplementary Figure 3. Effect of CZM on proteasome activity.** Parental H4 cells were
999 treated either with the vehicle (DMSO; Control), CZM or MG132, for 90 min. Protein
1000 extracts were used to measure *in vitro* the Chymotrypsin-like peptidase activity of the
1001 proteasome. The enzymatic activity was quantified according to the cleavage of the
1002 fluorogenic substrate Suc-LLVY-AMC to AMC, and normalized to that of control cells.
1003 The statistical significance was determined by One-Way ANOVA, followed by Tukey's
1004 test. Bars represent the mean ± SD of biological replicates (n=3). **P <0.01; n.s., not
1005 significant.

1006 **Supplementary Figure 4. Effect of CZM and MG132 on basal macroautophagy. (A)**
1007 Immunofluorescence microscopy analysis of the subcellular localization of LC3 in parental
1008 H4 cells treated with either with the vehicle (DMSO; Control), CZM for 4 h or MG132 for
1009 6 h. Cells were fixed, permeabilized and stained with a rabbit polyclonal antibody to LC3B
1010 followed by Alexa-594-conjugated donkey anti-Rabbit IgG. Scale bar 10 µm. **(B)** Parental
1011 H4 cells were treated as in (A) and protein extracts were analyzed by western blot with a
1012 polyclonal antibody to LC3B. Monoclonal antibody to β-actin (clone BA3R) was used as a
1013 loading control. The position of molecular mass markers is indicated on the left. **(C)** Ratio
1014 LC3B-II/LC3B-I ratio as shown in (B). The statistical significance was determined by One-

1015 Way ANOVA, followed by Tukey's test. Bars represent the mean ± SD of biological
1016 replicates (n=3). ***P <0.001; n.s., not significant.

1017 **Supplementary Figure 5. Distribution of RAB1A upon CZM treatment.**
1018 Immunofluorescence analysis of endogenous RAB1A in H4 parental cells treated either
1019 with vehicle (DMSO; Control) **(A-C)** or CZM for 4 h **(D-F)**. Cells were fixed,
1020 permeabilized, and double stained with a rabbit monoclonal antibody to RAB1A (clone
1021 D3X9S) (A and D) and a mouse monoclonal antibody to GM130 (clone35/GM130) (B and
1022 E), followed by Alexa-594-conjugated donkey anti-Rabbit IgG and Alexa-488-conjugated
1023 donkey anti-Mouse IgG. Merging of the images generated the third picture (C and F). Scale
1024 bar, 10 μm. **(G)** Quantitative analysis of the fraction of RAB1A colocalizing with GM130
1025 under CZM treatment and compared to control cells. The statistical significance was
1026 determined by Student's t-test. Bars represent the mean ± SEM of the fluorescent signal per
1027 cell area (n=173 cells). *P< 0.05.

1028 **Supplementary Figure 6. ATG9A is distributed in the swollen Golgi apparatus upon**
1029 **CZM treatment.** Immunofluorescence analysis of endogenous ATG9A in H4 parental
1030 cells treated either with the vehicle (DMSO; Control) **(A-C)** or CZM for 4 h **(D-F)**. Cells
1031 were fixed, permeabilized, and double stained with a rabbit monoclonal antibody to
1032 ATG9A (clone EPR2450(2)) (A and D) and a mouse monoclonal antibody to GM130
1033 (clone35/GM130) (B and E), followed by Alexa-594-conjugated donkey anti-Rabbit IgG
1034 and Alexa-488-conjugated donkey anti-Mouse IgG. Merging of the images generated the
1035 third picture (C and F). Scale bar, 10 μm. **(G)** Quantitative analysis of the fraction of
1036 ATG9A colocalizing with GM130 under CZM treatment and compared to control cells.
1037 The statistical significance was determined by Student's t-test. Bars represent the mean ±
1038 SEM of the fluorescent signal per cell area (n=93 cells). **P <0.01.

1039 **Supplementary Figure 7. siRNA sequences directed against human PSMD14 used for**
1040 **Validation Stage.**

1041 **Supplementary Figure 8. Primer pairs sequences used for RT-qPCR.**
1042